

Novel features of asymmetric nuclear matter from large neutron skin thickness and small neutron-star radii

Tsuyoshi Miyatsu^{1,*}, Myung-Ki Cheoun¹, Kyungsik Kim² and Koichi Saito³

¹*Department of Physics and OMEG Institute, Soongsil University, Seoul 06978, Republic of Korea*

²*School of Liberal Arts and Sciences, Korea Aerospace University, Goyang 10540, Republic of Korea*

³*Department of Physics and Astronomy, Faculty of Science and Technology, Tokyo University of Science, Noda 278-8510, Japan*

Correspondence*:

Tsuyoshi Miyatsu

tsuyoshi.miyatsu@ssu.ac.kr

ABSTRACT

The accurate measurement of neutron skin thickness of ^{208}Pb by the PREX Collaboration suggests a large value of the nuclear symmetry energy slope parameter, L , whereas the smaller L is preferred to account for the small neutron-star radii from NICER observations. To resolve this discrepancy between nuclear experiments and astrophysical observations, new effective interactions have been developed using relativistic mean-field models with the isoscalar- and isovector-meson mixing. We investigate the effects of δ -nucleon coupling and σ - δ mixing on the ground-state properties of finite nuclei, as well as the characteristics of isospin-asymmetric nuclear matter and neutron stars. Additionally, we explore the role of the quartic ρ -meson self-interaction in dense nuclear matter to mitigate the stiff equation of state for neutron stars resulting from the large δ -nucleon coupling. It is found that the nuclear symmetry energy undergoes a sudden softening at approximately twice the saturation density of nuclear matter, taking into account the PREX-2 result, the recent NICER observation of PSR J0437–4715, and the binary neutron star merger, GW170817.

Keywords: isospin-asymmetric nuclear matter, neutron skin thickness, neutron stars, NICER, nuclear equation of state, nuclear symmetry energy, PREX-2, relativistic mean-field models

1 INTRODUCTION

The astrophysical phenomena concerning compact stars as well as the characteristics of finite nuclei and nuclear matter are determined by the nuclear equation of state (EoS), characterized by the relation between the energy density and pressure of the system (Baym et al., 1971; Bethe et al., 1979). Many nuclear EoSs have been contemplated so far through realistic nuclear models in a nonrelativistic or relativistic framework (Lattimer and Swesty, 1991; Glendenning and Moszkowski, 1991). Relativistic mean-field (RMF) calculations, based on the one-boson exchange potential for nuclear interactions (Machleidt et al., 1987; Machleidt, 1989), have achieved great success in understanding of the properties of nuclear matter

and finite nuclei (Serot and Walecka, 1986). The RMF approach is, at present, one of the most powerful tools to study neutron star physics (Oertel et al., 2017; Alford et al., 2022; Patra et al., 2023), as in the case of the Skyrme energy density functional (Stone, 2021, 2024; Zhou et al., 2023; Sun et al., 2024).

The nuclear symmetry energy, E_{sym} , which is defined as the difference between the energies of pure neutron and symmetric nuclear matter, is recognized to be an important physical quantity to study the properties of isospin-asymmetric nuclear EoS (Li et al., 2008; Lattimer, 2014). In addition, the slope parameter of nuclear symmetry energy, L , gives a significant constraint on the density dependence of E_{sym} and is related to the neutron skin thickness of heavy nuclei (Typel and Brown, 2001). Laboratory experiments have been also performed to investigate the properties of low-density nuclear matter and to impose constraints on E_{sym} and L through the heavy-ion collisions (HICs) (Tsang et al., 2009, 2012). Recently, the impacts of the higher-order coefficients—the curvature and skewness of nuclear symmetry energy, K_{sym} and J_{sym} —have been studied in light of some astrophysical observations, for instance the mass-radius relations of neutron stars and the cooling process of proto-neutron stars (Zhang and Li, 2021; Richter and Li, 2023; Xie et al., 2024).

Owing to the precise observations of neutron stars, such as the Shapiro delay measurement of a binary millisecond pulsar J1614–2230 (Demorest et al., 2010; Arzoumanian et al., 2018) and the radius measurement of PSR J0740+6620 from Neutron Star Interior Composition Explorer (NICER) and from X-ray Multi-Mirror (XMM-Newton) Data (Miller et al., 2019, 2021; Riley et al., 2019, 2021), theoretical studies have been currently performed more than ever to elucidate neutron star physics through the nuclear EoS for dense matter. It has been found that the nuclear EoS should satisfy at least $2M_{\odot}$ to support the high-mass PSR J0740+6620 event, and that the precise measurements of neutron-star radii provide the valuable information in determining the features of isospin-asymmetric nuclear matter. In addition, the direct detection of gravitational-wave (GW) signals from a binary neutron star merger, GW170817, observed by Advanced LIGO and Advanced Virgo detectors has placed stringent restrictions on the mass–radius relation of neutron stars (Abbott et al., 2017, 2018, 2019). In particular, the tidal deformability of a neutron star (Hinderer, 2008; Hinderer et al., 2010) plays a critical role in constructing the EoS for neutron star matter (Annala et al., 2018; Lim and Holt, 2018; Most et al., 2018; Raithel et al., 2018). It has been reported that there are the strong correlations of neutron-star radii with E_{sym} and L , and the radius of a typical neutron star is determined by L (Alam et al., 2016; Hu et al., 2020; Li and Magno, 2020; Lopes, 2024). Using a Bayesian analysis based on constraints from NICER and GW170817 within chiral effective field theory calculations, L is currently estimated as $L = (43.7\text{--}70.0)$ MeV (Lim and Schwenk, 2024).

The accurate measurement of neutron skin thickness of ^{208}Pb , R_{skin}^{208} , by the PREX Collaboration, using the parity-violating electron scattering, has revealed a serious discrepancy between the measured R_{skin}^{208} and theoretical predictions (Adhikari et al., 2021). To explain the PREX-2 result, Reed et al. (2021) have proposed the large L value as $L = 106 \pm 37$ MeV, by exploiting the strong correlation between R_{skin}^{208} and L . In contrast, Reinhard et al. (2021), using modern relativistic and nonrelativistic energy density functionals, have predicted the smaller value, $L = 54 \pm 8$ MeV, by carefully assessing theoretical uncertainty on the parity-violating asymmetry, A_{PV} , in ^{208}Pb . Additionally, the CREX experiment, which provides a precise measurement of the neutron skin thickness of ^{48}Ca , R_{skin}^{48} , through the parity-violating electron scattering (Adhikari et al., 2022), complicates the understanding of isospin-asymmetric nuclear matter. This complexity arises from the difficulty of reconciling the PREX-2 and CREX results simultaneously.

In this article, we review the recently updated RMF models with nonlinear couplings by introducing the isoscalar- and isovector-meson mixing, $\sigma^2\delta^2$ and $\omega_{\mu}\omega^{\mu}\rho_{\nu}\rho^{\nu}$, which can cover both data from stable nuclear ground states and astrophysical observations of neutron stars. Although the isovector, Lorentz-scalar (δ)

meson has been claimed to be less important than the isovector, Lorentz-vector (ρ^μ) meson so far, it has been recently realized that the δ meson considerably affects the properties of isospin-asymmetric nuclear EoS, such as neutron skin thickness of heavy nuclei and neutron-star radii (Zabari et al., 2019; Miyatsu et al., 2022b, 2023; Li et al., 2022) The new effective interactions discussed in this review are constructed under the constraints from the terrestrial experiments and astrophysical observations of neutron stars, especially focusing on the PREX-2 and CREX experiments. The resulting nuclear EoS have to support the following conditions:

- (1) the EoSs for symmetric nuclear matter and pure neutron matter satisfy the particle flow data in heavy-ion collisions (HICs) (Danielewicz et al., 2002; Fuchs, 2006; Lynch et al., 2009; Oliinychenko et al., 2023),
- (2) the EoS for neutron stars attains to the observed mass of PSR J0740+6620 ($M = 2.072_{-0.066}^{+0.067} M_\odot$) (Cromartie et al., 2019; Fonseca et al., 2021; Riley et al., 2021),
- (3) the EoS for neutron stars explains the dimensionless tidal deformability from the binary merger event, GW170817 ($\Lambda_{1.4} = 190_{-120}^{+390}$) (Abbott et al., 2018, 2019).

Under these constraints, we examine the effects of the δ -nucleon coupling and σ - δ mixing on the ground-state properties of finite nuclei, and consider the PREX-2 and CREX results. Additionally, we investigate the impact of the quartic self-interactions of δ and ρ mesons on the nuclear EoS to study the properties of neutron star matter.

This paper is organized as follows. A summary and analytical calculations concerning the RMF model with nonlinear couplings are described in Sec. 2. Numerical results and detailed discussions are presented in Sec. 3. Finally, we give a summary in Sec. 4.

2 THEORETICAL FRAMEWORK

2.1 Lagrangian density

In quantum hadrodynamics (Serot and Walecka, 1986), we employ the recently updated effective Lagrangian density including the isoscalar (σ and ω^μ) and isovector (δ and ρ^μ) mesons as well as nucleons ($N = p, n$) (Miyatsu et al., 2022b, 2023). The total Lagrangian density is then given by

$$\begin{aligned} \mathcal{L} = & \bar{\psi}_N [i\gamma_\mu \partial^\mu - (M_N - g_\sigma \sigma - g_\delta \boldsymbol{\delta} \cdot \boldsymbol{\tau}_N) - g_\omega \gamma_\mu \omega^\mu - g_\rho \gamma_\mu \boldsymbol{\rho}^\mu \cdot \boldsymbol{\tau}_N] \psi_N \\ & + \frac{1}{2} (\partial_\mu \sigma \partial^\mu \sigma - m_\sigma^2 \sigma^2) + \frac{1}{2} m_\omega^2 \omega_\mu \omega^\mu - \frac{1}{4} W_{\mu\nu} W^{\mu\nu} + \frac{1}{2} (\partial_\mu \boldsymbol{\delta} \cdot \partial^\mu \boldsymbol{\delta} - m_\delta^2 \boldsymbol{\delta} \cdot \boldsymbol{\delta}) \\ & + \frac{1}{2} m_\rho^2 \boldsymbol{\rho}_\mu \cdot \boldsymbol{\rho}^\mu - \frac{1}{4} \mathbf{R}_{\mu\nu} \cdot \mathbf{R}^{\mu\nu} + \mathcal{L}_{\text{EM}} - U_{\text{NL}}(\sigma, \omega, \boldsymbol{\delta}, \boldsymbol{\rho}), \end{aligned} \quad (1)$$

where $\psi_N = \begin{pmatrix} \psi_p \\ \psi_n \end{pmatrix}$ is the iso-doublet, nucleon field, $\boldsymbol{\tau}_N$ is its isospin matrix, $W_{\mu\nu} = \partial_\mu \omega_\nu - \partial_\nu \omega_\mu$, and $\mathbf{R}_{\mu\nu} = \partial_\mu \boldsymbol{\rho}_\nu - \partial_\nu \boldsymbol{\rho}_\mu$. The meson-nucleon coupling constants are respectively denoted by g_σ , g_ω , g_δ , and g_ρ . The photon- N interaction, $\mathcal{L}_{\text{EM}} = -e\bar{\psi}_p \gamma_\mu A^\mu \psi_p - \frac{1}{4} F_{\mu\nu} F^{\mu\nu}$ with $F_{\mu\nu} = \partial_\mu A_\nu - \partial_\nu A_\mu$, is also taken into account to describe the characteristics of finite nuclei (Serot and Walecka, 1986; Ring, 1996).

Additionally, a nonlinear potential in Eq. (1) is supplemented as follows:

$$U_{\text{NL}}(\sigma, \omega, \boldsymbol{\delta}, \boldsymbol{\rho}) = \frac{1}{3}g_2\sigma^3 + \frac{1}{4}g_3\sigma^4 - \frac{1}{4}c_3(\omega_\mu\omega^\mu)^2 + \frac{1}{4}d_3(\boldsymbol{\delta} \cdot \boldsymbol{\delta})^2 - \frac{1}{4}e_3(\boldsymbol{\rho}_\mu \cdot \boldsymbol{\rho}^\mu)^2 - \Gamma_{\sigma\delta}\sigma(\boldsymbol{\delta} \cdot \boldsymbol{\delta}) - \Lambda_{\sigma\delta}\sigma^2(\boldsymbol{\delta} \cdot \boldsymbol{\delta}) - \Lambda_{\omega\rho}(\omega_\mu\omega^\mu)(\boldsymbol{\rho}_\nu \cdot \boldsymbol{\rho}^\nu). \quad (2)$$

The first and second terms in Eq. (2) are introduced to obtain a quantitative description of ground-state properties for symmetric nuclear matter (Boguta and Bodmer, 1977; Lalazissis et al., 1997). The quartic self-interactions of ω , δ , and ρ mesons are also introduced in Eq. (2) (Sugahara and Toki, 1994; Mueller and Serot, 1996; Pradhan et al., 2023; Malik et al., 2024). We also consider the isoscalar- and isovector-meson mixing, which only affects the characteristics of $N \neq Z$ finite nuclei and isospin-asymmetric nuclear matter (Todd-Rutel and Piekarewicz, 2005; Miyatsu et al., 2013a; Zabari et al., 2019), while the scalar-vector mixing is not included in the present study (Horowitz and Piekarewicz, 2001a,b; Haidari and Sharma, 2008; Sharma, 2008; Kubis et al., 2023).

2.2 Field equations for finite nuclei in mean-field approximation

In mean-field approximation, the meson and photon fields are replaced by the mean-field values: $\bar{\sigma}$, $\bar{\omega}$, $\bar{\delta}$, $\bar{\rho}$, and \bar{A} . Then, the effective nucleon mass in matter is simply expressed as

$$M_{N=(\begin{smallmatrix} p \\ n \end{smallmatrix})}^*(\bar{\sigma}, \bar{\delta}) = M_N - g_\sigma\bar{\sigma} \mp g_\delta\bar{\delta}, \quad (3)$$

where M_N ($= 939$ MeV) is the nucleon mass in free space. If we restrict consideration to spherical finite nuclei, the equation of motion for N is given by

$$\left[-i\boldsymbol{\alpha} \cdot \boldsymbol{\nabla} + \beta M_{N=(\begin{smallmatrix} p \\ n \end{smallmatrix})}^*(\bar{\sigma}, \bar{\delta}) + g_\omega\bar{\omega} \pm g_\rho\bar{\rho} + e\frac{1 \pm 1}{2}\bar{A} \right] \psi_{N=(\begin{smallmatrix} p \\ n \end{smallmatrix})} = E_{\alpha N} \psi_{N=(\begin{smallmatrix} p \\ n \end{smallmatrix})}, \quad (4)$$

with $E_{\alpha N}$ being the nucleon single-particle energy. The meson and photon fields are then given by

$$[-\nabla^2 + m_\sigma^{*2}(\bar{\sigma}, \bar{\delta})] \bar{\sigma} = g_\sigma (\rho_p^s + \rho_n^s), \quad (5)$$

$$[-\nabla^2 + m_\omega^{*2}(\bar{\omega}, \bar{\rho})] \bar{\omega} = g_\omega (\rho_p + \rho_n), \quad (6)$$

$$[-\nabla^2 + m_\delta^{*2}(\bar{\sigma}, \bar{\delta})] \bar{\delta} = g_\delta (\rho_p^s - \rho_n^s), \quad (7)$$

$$[-\nabla^2 + m_\rho^{*2}(\bar{\omega}, \bar{\rho})] \bar{\rho} = g_\rho (\rho_p - \rho_n), \quad (8)$$

$$-\nabla^2 \bar{A} = e\rho_p, \quad (9)$$

where ρ_N^s (ρ_N) is the scalar (baryon) density for N , and the effective meson masses are defined by

$$m_\sigma^{*2}(\bar{\sigma}, \bar{\delta}) = m_\sigma^2 + g_2\bar{\sigma} + g_3\bar{\sigma}^2 - \Gamma_{\sigma\delta}\bar{\delta}^2/\bar{\sigma} - 2\Lambda_{\sigma\delta}\bar{\delta}^2, \quad (10)$$

$$m_\omega^{*2}(\bar{\omega}, \bar{\rho}) = m_\omega^2 + c_3\bar{\omega}^2 + 2\Lambda_{\omega\rho}\bar{\rho}^2, \quad (11)$$

$$m_\delta^{*2}(\bar{\sigma}, \bar{\delta}) = m_\delta^2 + d_3\bar{\delta}^2 - 2\Gamma_{\sigma\delta}\bar{\sigma} - 2\Lambda_{\sigma\delta}\bar{\sigma}^2, \quad (12)$$

$$m_\rho^{*2}(\bar{\omega}, \bar{\rho}) = m_\rho^2 + e_3\bar{\rho}^2 + 2\Lambda_{\omega\rho}\bar{\omega}^2. \quad (13)$$

The total energy of the system is thus written as

$$\begin{aligned}
 E_{\text{tot}} = & \sum_{N=p,n} \sum_{\alpha}^{\text{occ}} (2j_{\alpha} + 1) E_{\alpha N} \\
 & + \frac{1}{2} \int d\mathbf{r} \left[g_{\sigma} (\rho_p^s + \rho_n^s) \bar{\sigma} - g_{\omega} (\rho_p + \rho_n) \bar{\omega} + g_{\delta} (\rho_p^s - \rho_n^s) \bar{\delta} - g_{\rho} (\rho_p - \rho_n) \bar{\rho} - e_{\rho p} \bar{A} \right] \\
 & + \frac{1}{2} \int d\mathbf{r} \left[-\frac{1}{3} g_2 \bar{\sigma}^3 - \frac{1}{2} g_3 \bar{\sigma}^4 + \frac{1}{2} c_3 \bar{\omega}^4 - \frac{1}{2} d_3 \bar{\delta}^4 + \frac{1}{2} e_3 \bar{\rho}^4 + \Gamma_{\sigma\delta} \bar{\sigma} \bar{\delta}^2 + 2\Lambda_{\sigma\delta} \bar{\sigma}^2 \bar{\delta}^2 + 2\Lambda_{\omega\rho} \bar{\omega}^2 \bar{\rho}^2 \right], \quad (14)
 \end{aligned}$$

where the sum α runs over the occupied states of $E_{\alpha N}$ with the degeneracy $(2j_{\alpha} + 1)$ (Serot and Walecka, 1986).

2.3 Infinite nuclear matter

To study the bulk properties of nuclear and neutron star matter, it is necessary to compute the nuclear equation of state (EoS)—a relation between the energy density, ε_B , and pressure, P_B . In infinite nuclear matter, the surface terms in Eqs. (5)–(9) have no influence on its characteristics as the gradient reads zero. The scalar and baryon density for N ($= p, n$) are then obtained as

$$\rho_N^s = \frac{1}{\pi^2} \int_0^{k_{FN}} dk k^2 \frac{M_N^*}{\sqrt{k^2 + M_N^{*2}}} = \frac{M_N^{*3}}{2\pi^2} \left[\frac{k_{FN} E_N^*}{M_N^{*2}} - \ln \left(\frac{k_{FN} + E_N^*}{M_N^*} \right) \right], \quad (15)$$

$$\rho_N = \frac{1}{\pi^2} \int_0^{k_{FN}} dk k^2 = \frac{k_{FN}^3}{3\pi^2}, \quad (16)$$

where k_{FN} and E_N^* ($= \sqrt{k_{FN}^2 + M_N^{*2}}$) are the Fermi momentum and energy for N . With the self-consistent calculations of the meson fields, ε_B and P_B are respectively given by $\varepsilon_B = \sum_N \varepsilon_N + \varepsilon_M$ and $P_B = \sum_N P_N + P_M$ where the nucleon and meson parts are expressed as

$$\varepsilon_N = \frac{1}{\pi^2} \int_0^{k_{FN}} dk k^2 \sqrt{k^2 + M_N^{*2}} = \frac{1}{4} (3E_N^* \rho_N + M_N^* \rho_N^s), \quad (17)$$

$$P_N = \frac{1}{\pi^2} \int_0^{k_{FN}} dk \frac{k^4}{\sqrt{k^2 + M_N^{*2}}} = \frac{1}{4} (E_N^* \rho_N - M_N^* \rho_N^s), \quad (18)$$

and

$$\begin{aligned}
 \varepsilon_M = & \frac{1}{2} (m_{\sigma}^2 \bar{\sigma}^2 + m_{\omega}^2 \bar{\omega}^2 + m_{\delta}^2 \bar{\delta}^2 + m_{\rho}^2 \bar{\rho}^2) \\
 & + \frac{1}{3} g_2 \bar{\sigma}^3 + \frac{1}{4} g_3 \bar{\sigma}^4 + \frac{3}{4} c_3 \bar{\omega}^4 + \frac{1}{4} \bar{\delta}^4 + \frac{3}{4} e_3 \bar{\rho}^4 - \Gamma_{\sigma\delta} \bar{\sigma} \bar{\delta}^2 - \Lambda_{\sigma\delta} \bar{\sigma}^2 \bar{\delta}^2 + 3\Lambda_{\omega\rho} \bar{\omega}^2 \bar{\rho}^2, \quad (19)
 \end{aligned}$$

$$\begin{aligned}
 P_M = & -\frac{1}{2} (m_{\sigma}^2 \bar{\sigma}^2 - m_{\omega}^2 \bar{\omega}^2 + m_{\delta}^2 \bar{\delta}^2 - m_{\rho}^2 \bar{\rho}^2) \\
 & - \frac{1}{3} g_2 \bar{\sigma}^3 - \frac{1}{4} g_3 \bar{\sigma}^4 + \frac{1}{4} c_3 \bar{\omega}^4 - \frac{1}{4} \bar{\delta}^4 + \frac{1}{4} e_3 \bar{\rho}^4 + \Gamma_{\sigma\delta} \bar{\sigma} \bar{\delta}^2 + \Lambda_{\sigma\delta} \bar{\sigma}^2 \bar{\delta}^2 + \Lambda_{\omega\rho} \bar{\omega}^2 \bar{\rho}^2. \quad (20)
 \end{aligned}$$

2.4 Nuclear bulk properties

In general, the bulk properties of infinite nuclear matter are identified by the expansion of isospin-asymmetric nuclear EoS with a power series in the isospin asymmetry, $\alpha = (\rho_n - \rho_p)/\rho_B$, and the total baryon density, $\rho_B (= \rho_n + \rho_p)$ (Chen et al., 2007, 2009). The binding energy per nucleon is then written as

$$\begin{aligned} E_B(\rho_B, \alpha) &= \frac{\varepsilon_B(\rho_B, \alpha)}{\rho_B} - M_N \\ &= E_0(\rho_B) + E_{\text{sym}}(\rho_B)\alpha^2 + \mathcal{O}(\alpha^4), \end{aligned} \quad (21)$$

where $E_0(\rho_B)$ is the binding energy per nucleon of symmetric nuclear matter (SNM) and $E_{\text{sym}}(\rho_B)$ is the nuclear symmetry energy (NSE),

$$E_{\text{sym}}(\rho_B) = \frac{1}{2} \left. \frac{\partial^2 E_B(\rho_B, \alpha)}{\partial \alpha^2} \right|_{\alpha=0}. \quad (22)$$

Besides, $E_0(\rho_B)$ and $E_{\text{sym}}(\rho_B)$ can be expanded around the nuclear saturation density, ρ_0 , as

$$E_0(\rho_B) = E_0(\rho_0) + \frac{K_0}{2}\chi^2 + \frac{J_0}{6}\chi^3 + \mathcal{O}(\chi^4), \quad (23)$$

$$E_{\text{sym}}(\rho_B) = E_{\text{sym}}(\rho_0) + L\chi + \frac{K_{\text{sym}}}{2}\chi^2 + \frac{J_{\text{sym}}}{6}\chi^3 + \mathcal{O}(\chi^4), \quad (24)$$

with $\chi = (\rho_B - \rho_0)/3\rho_0$ being the dimensionless variable characterizing the deviations of ρ_B from ρ_0 . The incompressibility coefficient of SNM, K_0 , the slope and curvature parameters of NSE, L and K_{sym} , and the third-order incompressibility coefficients of SNM and NSE, J_0 and J_{sym} , are respectively defined as

$$K_0 = 9\rho_0^2 \left. \frac{d^2 E_0(\rho_B)}{d\rho_B^2} \right|_{\rho_B=\rho_0}, \quad (25)$$

$$L = 3\rho_0 \left. \frac{dE_{\text{sym}}(\rho_B)}{d\rho_B} \right|_{\rho_B=\rho_0}, \quad K_{\text{sym}} = 9\rho_0^2 \left. \frac{d^2 E_{\text{sym}}(\rho_B)}{d\rho_B^2} \right|_{\rho_B=\rho_0}, \quad (26)$$

$$J_0 = 27\rho_0^3 \left. \frac{d^3 E_0(\rho_B)}{d\rho_B^3} \right|_{\rho_B=\rho_0}, \quad J_{\text{sym}} = 27\rho_0^3 \left. \frac{d^3 E_{\text{sym}}(\rho_B)}{d\rho_B^3} \right|_{\rho_B=\rho_0}. \quad (27)$$

Taking into account the thermodynamic condition, the pressure of infinite nuclear matter, $P_B(\rho_B, \alpha)$, is given by

$$\begin{aligned} P_B(\rho_B, \alpha) &= \rho_B^2 \frac{\partial E_B(\rho_B, \alpha)}{\partial \rho_B} \\ &= \rho_B^2 \frac{\partial}{\partial \rho_B} \left[\frac{\varepsilon_B(\rho_B, \alpha)}{\rho_B} - M_N \right] \\ &= \rho_B \frac{\partial \varepsilon_B(\rho_B, \alpha)}{\partial \rho_B} - \varepsilon_B(\rho_B, \alpha), \end{aligned} \quad (28)$$

with the binding energy per nucleon in Eq. (21). The nuclear incompressibility, $K_B(\rho_B, \alpha)$, is then expressed as

$$\begin{aligned} K_B(\rho_B, \alpha) &= 9\rho_B^2 \frac{\partial^2 E_B(\rho_B, \alpha)}{\partial \rho_B^2} \\ &= 9\rho_B^2 \frac{\partial}{\partial \rho_B} \left[\frac{P_B(\rho_B, \alpha)}{\rho_B^2} \right] \\ &= 9 \left[\frac{\partial P_B(\rho_B, \alpha)}{\partial \rho_B} - 2 \frac{P_B(\rho_B, \alpha)}{\rho_B} \right]. \end{aligned} \quad (29)$$

Hence, the incompressibility coefficient of SNM, K_0 , in Eq. (25) is related with K_B through $K_0 = K_B(\rho_0, 0)$. In the RMF calculation, we can obtain the analytical expression of $K_B(\rho_B, \alpha)$ using the following equation:

$$\begin{aligned} \frac{\partial P_B}{\partial \rho_B} &= \frac{1}{3\rho_B} \sum_{N=p,n} \rho_N \frac{k_{FN}^2}{E_N^*} \\ &\quad - \sum_{N=p,n} \rho_N \frac{M_N^*}{E_N^*} \left[g_\sigma \frac{\partial \bar{\sigma}}{\partial \rho_B} + g_\delta (\boldsymbol{\tau}_N)_3 \frac{\partial \bar{\delta}}{\partial \rho_B} \right] + m_\omega^{*2} \bar{\omega} \frac{\partial \bar{\omega}}{\partial \rho_B} + m_\rho^{*2} \bar{\rho} \frac{\partial \bar{\rho}}{\partial \rho_B}, \end{aligned} \quad (30)$$

where the density derivatives of meson fields are calculated through the relation

$$\frac{\partial \mathcal{M}}{\partial \rho_B} = \sum_{N=p,n} \frac{\rho_N}{\rho_B} \frac{\partial \mathcal{M}}{\partial \rho_N} \quad (\mathcal{M} = \bar{\sigma}, \bar{\omega}, \bar{\delta}, \bar{\rho}), \quad (31)$$

with

$$\frac{\partial \bar{\sigma}}{\partial \rho_N} = \frac{M_N^*}{E_N^*} \frac{G_\sigma + G_\delta (\boldsymbol{\tau}_N)_3 H_{\sigma\delta}}{1 - H_{\sigma\delta} H_{\delta\sigma}}, \quad \frac{\partial \bar{\omega}}{\partial \rho_N} = \frac{G_\omega - G_\rho (\boldsymbol{\tau}_N)_3 H_{\omega\rho}}{1 - H_{\omega\rho} H_{\rho\omega}}, \quad (32)$$

$$\frac{\partial \bar{\delta}}{\partial \rho_N} = \frac{M_N^*}{E_N^*} \frac{G_\sigma H_{\delta\sigma} + G_\delta (\boldsymbol{\tau}_N)_3}{1 - H_{\sigma\delta} H_{\delta\sigma}}, \quad \frac{\partial \bar{\rho}}{\partial \rho_N} = \frac{-G_\omega H_{\rho\omega} + G_\rho (\boldsymbol{\tau}_N)_3}{1 - H_{\omega\rho} H_{\rho\omega}}, \quad (33)$$

and

$$(\boldsymbol{\tau}_N)_3 = \begin{cases} +1 \\ -1 \end{cases} \quad \text{for } N = \begin{pmatrix} p \\ n \end{pmatrix}. \quad (34)$$

We here use the following quantities:

$$G_\sigma = \frac{g_\sigma}{M_\sigma^2}, \quad G_\omega = \frac{g_\omega}{M_\omega^2}, \quad G_\delta = \frac{g_\delta}{M_\delta^2}, \quad G_\rho = \frac{g_\rho}{M_\rho^2}, \quad (35)$$

and

$$H_{\sigma\delta} = \frac{L_{\sigma\delta}^2}{M_\sigma^2}, \quad H_{\delta\sigma} = \frac{L_{\sigma\delta}^2}{M_\delta^2}, \quad H_{\omega\rho} = \frac{4\Lambda_{\omega\rho} \bar{\omega} \bar{\rho}}{M_\omega^2}, \quad H_{\rho\omega} = \frac{4\Lambda_{\omega\rho} \bar{\omega} \bar{\rho}}{M_\rho^2}, \quad (36)$$

with

$$M_\sigma^2(\bar{\sigma}, \bar{\delta}) = m_\sigma^{*2}(\bar{\sigma}, \bar{\delta}) + g_2\bar{\sigma} + 2g_3\bar{\sigma}^2 + \Gamma_{\sigma\delta}\bar{\delta}^2/\bar{\sigma} + g_\sigma^2(J_p + J_n), \quad (37)$$

$$M_\omega^2(\bar{\omega}, \bar{\rho}) = m_\omega^{*2}(\bar{\omega}, \bar{\rho}) + 2c_3\bar{\omega}^2, \quad (38)$$

$$M_\delta^2(\bar{\sigma}, \bar{\delta}) = m_\delta^{*2}(\bar{\sigma}, \bar{\delta}) + 2d_3\bar{\delta}^2 + g_\delta^2(J_p + J_n), \quad (39)$$

$$M_\rho^2(\bar{\omega}, \bar{\rho}) = m_\rho^{*2}(\bar{\omega}, \bar{\rho}) + 2e_3\bar{\rho}^2, \quad (40)$$

$$L_{\sigma\delta}^2(\bar{\sigma}, \bar{\delta}) = 2\Gamma_{\sigma\delta}\bar{\delta} + 4\Lambda_{\sigma\delta}\bar{\sigma}\bar{\delta} - g_\sigma g_\delta (J_p - J_n), \quad (41)$$

where the effective meson masses, m_σ^{*2} , m_ω^{*2} , m_δ^{*2} and m_ρ^{*2} , are given in Eqs. (10)–(13), and J_N for N ($= p, n$) reads

$$J_N = 3 \left(\frac{\rho_N^s}{M_N^*} - \frac{\rho_N}{E_N^*} \right). \quad (42)$$

According to the Hugenholtz-Van Hove theorem in nuclear matter, E_{sym} defined in Eq. (22) can be generally written as

$$\begin{aligned} E_{\text{sym}}(\rho_B) &= \frac{1}{2} \frac{\partial}{\partial \alpha} \left[\frac{\partial E_B(\rho_B, \alpha)}{\partial \alpha} \right]_{\alpha=0} \\ &= \frac{1}{8} \rho_B \left(\frac{\partial}{\partial \rho_p} - \frac{\partial}{\partial \rho_n} \right) [E_p(k_{F_p}) - E_n(k_{F_n})] \Big|_{\rho_p=\rho_n}, \end{aligned} \quad (43)$$

where E_N is the single-particle energy for N , which is determined self-consistently by solving the following transcendental equation (Czerski et al., 2002; Cai and Chen, 2012):

$$E_N(k) = [E_N^*(k) - \Sigma_N^0(k)]_{k^0=E_N(k)}. \quad (44)$$

The effective mass, (four) momentum, and energy for N are here defined as (Miyatsu et al., 2012; Katayama et al., 2012)

$$M_N^*(k) = M_N + \Sigma_N^s(k), \quad (45)$$

$$\begin{aligned} k_N^{\mu*} &= (k_N^{*0}, \mathbf{k}_N^*) \\ &= (k^0 + \Sigma_N^0(k), \mathbf{k} + \hat{k}\Sigma_N^v(k)), \end{aligned} \quad (46)$$

$$E_N^*(k) = \sqrt{\mathbf{k}_N^{*2} + M_N^{*2}(k)}, \quad (47)$$

with $\Sigma_N^{s(0)[v]}$ being the scalar (time) [space] component of nucleon self-energy. In addition, E_{sym} is divided into the kinetic and potential terms as

$$E_{\text{sym}}(\rho_B) = E_{\text{sym}}^{\text{kin}}(\rho_B) + E_{\text{sym}}^{\text{pot}}(\rho_B). \quad (48)$$

Based on the Lorentz-covariant decomposition of NSE (Miyatsu et al., 2020), $E_{\text{sym}}^{\text{pot}}$ is expressed as

$$E_{\text{sym}}^{\text{pot}}(\rho_B) = E_{\text{sym}}^s(\rho_B) + E_{\text{sym}}^0(\rho_B) + E_{\text{sym}}^v(\rho_B), \quad (49)$$

with the scalar (s), time (0), and space (v) components. The E_{sym} is thus computed as follows:

$$E_{\text{sym}}^{\text{kin}}(\rho_B) = \frac{1}{6} \frac{k_F^*}{E_F^*} k_F, \quad (50)$$

$$E_{\text{sym}}^s(\rho_B) = \frac{1}{8} \rho_B \frac{M_F^*}{E_F^*} \left(\frac{\partial}{\partial \rho_p} - \frac{\partial}{\partial \rho_n} \right) (\Sigma_p^s - \Sigma_n^s) \Big|_{\rho_p=\rho_n}, \quad (51)$$

$$E_{\text{sym}}^0(\rho_B) = -\frac{1}{8} \rho_B \left(\frac{\partial}{\partial \rho_p} - \frac{\partial}{\partial \rho_n} \right) (\Sigma_p^0 - \Sigma_n^0) \Big|_{\rho_p=\rho_n}, \quad (52)$$

$$E_{\text{sym}}^v(\rho_B) = \frac{1}{8} \rho_B \frac{k_F^*}{E_F^*} \left(\frac{\partial}{\partial \rho_p} - \frac{\partial}{\partial \rho_n} \right) (\Sigma_p^v - \Sigma_n^v) \Big|_{\rho_p=\rho_n}, \quad (53)$$

where the effective quantities at the Fermi surface in Eq. (50)–(53) are then given by $M_F^* = M_p^*(k_F) = M_n^*(k_F)$, $k_F^* = |\mathbf{k}_p^*(k_F)| = |\mathbf{k}_n^*(k_F)|$, and $E_F^* = E_p^*(k_F) = E_n^*(k_F)$ at $\rho_p = \rho_n$, namely $k_{F_p} = k_{F_n} = k_F$. In RMF approximation, $\Sigma_N^{s,0,v}$ are respectively given by

$$\Sigma_N^s = -g_\sigma \bar{\sigma} - g_\delta (\boldsymbol{\tau}_N)_3 \bar{\delta}, \quad (54)$$

$$\Sigma_N^0 = -g_\omega \bar{\omega} - g_\rho (\boldsymbol{\tau}_N)_3 \bar{\rho}, \quad (55)$$

$$\Sigma_N^v = 0. \quad (56)$$

Using Eqs. (32) and (33), E_{sym} can be finally expressed as

$$\begin{aligned} E_{\text{sym}}(\rho_B) &= E_{\text{sym}}^{\text{kin}}(\rho_B) + E_{\text{sym}}^s(\rho_B) + E_{\text{sym}}^0(\rho_B) \\ &= \frac{1}{6} \frac{k_F^2}{E_F^*} - \frac{1}{2} \frac{g_\delta^2}{M_\delta^2(\bar{\sigma}, 0)} \left(\frac{M_F^*}{E_F^*} \right)^2 \rho_B + \frac{1}{2} \frac{g_\rho^2}{M_\rho^2(\bar{\omega}, 0)} \rho_B. \end{aligned} \quad (57)$$

Note that $k_F^* = k_F$ and $E_{\text{sym}}^v(\rho_B) = 0$ in RMF approximation.

The L and K_{sym} given in Eq. (26) are also expressed as

$$L = L^{\text{kin}} + L^{\text{pot}} = L^{\text{kin}} + L^s + L^0, \quad (58)$$

$$K_{\text{sym}} = K_{\text{sym}}^{\text{kin}} + K_{\text{sym}}^{\text{pot}} = K_{\text{sym}}^{\text{kin}} + K_{\text{sym}}^s + K_{\text{sym}}^0, \quad (59)$$

where the kinetic, scalar, and time components are respectively given by

$$L^{\text{kin}} = E_{\text{sym}}^{\text{kin}}(\rho_0) \left[1 + \left(\frac{M_F^*}{E_F^*} \right)^2 \mathcal{K}_B(\rho_0) \right], \quad (60)$$

$$L^{s(0)} = 3E_{\text{sym}}^{s(0)}(\rho_0) \left[1 - \rho_0 \mathcal{T}_B^{s(0)}(\rho_0) \right], \quad (61)$$

$$K_{\text{sym}}^{\text{kin}} = -2L^{\text{kin}} + \left(\frac{M_F^*}{E_F^*} \right)^2 \left[E_{\text{sym}}^{\text{kin}}(\rho_0) \mathcal{N}_B(\rho_0) + L^{\text{kin}} \mathcal{K}_B(\rho_0) \right], \quad (62)$$

$$K_{\text{sym}}^{s(0)} = 3L^{s(0)} \left[1 - \rho_0 \mathcal{T}_B^{s(0)}(\rho_0) \right] - 9E_{\text{sym}}^{s(0)} \left[1 + \rho_0^2 \frac{d\mathcal{T}_B^{s(0)}(\rho_B)}{d\rho_B} \Big|_{\rho_B=\rho_0} \right], \quad (63)$$

with

$$\mathcal{K}_B(\rho_B) = 1 + 3 \frac{g_\sigma^2}{M_\sigma^2(\bar{\sigma}, 0)} \frac{\rho_B}{E_F^*}, \quad (64)$$

$$\begin{aligned} \mathcal{T}_B^s(\rho_B) = & \frac{2}{3\rho_B} \left(\frac{k_F}{E_F^*} \right)^2 \mathcal{K}_B(\rho_B) - \frac{g_\sigma (2\Gamma_{\sigma\delta} + 4\Lambda_{\sigma\delta}\bar{\sigma})}{M_\sigma^2(\bar{\sigma}, 0)M_\delta^2(\bar{\sigma}, 0)} \frac{M_F^*}{E_F^*} \\ & + \frac{g_\delta^2}{M_\delta^2(\bar{\sigma}, 0)} \left[\left(\frac{k_F}{E_F^*} \right)^2 \frac{\mathcal{K}_B(\rho_B)}{E_F^*} - 2 \frac{g_\sigma^2}{M_\sigma^2(\bar{\sigma}, 0)} \frac{J_p + J_n}{E_F^*} \right], \end{aligned} \quad (65)$$

$$\mathcal{T}_B^0(\rho_B) = \frac{4g_\omega\Lambda_{\omega\rho}\bar{\omega}}{M_\omega^2(\bar{\omega}, 0)M_\rho^2(\bar{\omega}, 0)}, \quad (66)$$

$$\mathcal{N}_B(\rho_B) = 3\rho_B \frac{d\mathcal{K}_B(\rho_B)}{d\rho_B} - 2 \left(\frac{k_F}{E_F^*} \right)^2 \mathcal{K}_B^2(\rho_B). \quad (67)$$

2.5 Stability of nuclear and neutron star matter

In order to move on the calculations of neutron stars in which the charge neutrality and β equilibrium conditions are imposed, we introduce the degrees of freedom of leptons (electrons and muons) as well as nucleons and mesons in Eq. (1)

$$\mathcal{L}_L = \bar{\psi}_\ell (i\gamma_\mu \partial^\mu - \hat{m}_\ell) \psi_\ell, \quad (68)$$

where $\psi_\ell = \begin{pmatrix} \psi_e \\ \psi_\mu \end{pmatrix}$ is the lepton field and its mass is given by $\hat{m}_\ell = \text{diag}(m_e, m_\mu)$.

When we consider the stability of matter in cold neutron stars, the first principle of thermodynamics should be considered:

$$du = -Pdv - \mu dq, \quad (69)$$

with u , P , $v (= 1/\rho_B)$, μ , and q being the total internal energy per nucleon, pressure, volume per nucleon, chemical potential, and charge fraction, respectively (Kubis, 2007; Lattimer and Prakash, 2007; Xu et al., 2009; Moustakidis et al., 2010). In neutron star matter, the charge neutrality and β equilibrium conditions read

$$\mu = \mu_n - \mu_p = \mu_e = \mu_\mu, \quad (70)$$

$$q = Y_p - Y_L = \rho_p/\rho_B - \sum_{\ell=e,\mu} \rho_\ell/\rho_B = 0, \quad (71)$$

with ρ_ℓ the lepton density. The stability of neutron star matter are then expressed as the following two constraints on chemical potential and pressure:

$$- \left(\frac{\partial \mu}{\partial q} \right)_v > 0, \quad (72)$$

$$- \left(\frac{\partial P}{\partial v} \right)_\mu > 0. \quad (73)$$

The total internal energy per baryon, $u(v, q)$, can be decomposed into the baryon (B) and lepton (L) contributions as

$$\begin{aligned} u(v, q) &= u(\rho_B, \alpha) \\ &= E_B(\rho_B, \alpha) + E_L(\rho_B, \alpha), \end{aligned} \quad (74)$$

with $\alpha = 1 - 2Y_p$. At zero temperature, the β equilibrium condition leads to the relation (Psonis et al., 2007)

$$\begin{aligned} \mu &= - \left(\frac{\partial E_B}{\partial Y_p} \right)_{\rho_B} \\ &= 2 \left(\frac{\partial E_B}{\partial \alpha} \right)_{\rho_B} = 2E_{\text{ISB}}(\rho_B, \alpha). \end{aligned} \quad (75)$$

where the isospin symmetry breaking (ISB) energy of infinite nuclear matter is given by

$$\begin{aligned} E_{\text{ISB}}(\rho_B, \alpha) &= \left[\frac{\partial E_B(\rho_B, \alpha)}{\partial \alpha} \right]_{\rho_B} \\ &= \frac{1}{2} [E_n(k_{F_n}) - E_p(k_{F_p})]. \end{aligned} \quad (76)$$

Considering the differentiation of $\mu(v, q)$ ($= \mu(\rho_B, \alpha)$), we find

$$\begin{aligned} - \left(\frac{\partial q}{\partial \mu} \right)_v &= \frac{1}{2} \left(\frac{\partial \alpha}{\partial \mu} \right)_{\rho_B} + \frac{1}{\rho_B} \sum_{\ell=e, \mu} \left(\frac{\partial \rho_\ell}{\partial \mu} \right)_{\rho_B} \\ &= \frac{1}{8E_{\text{sym}}(\rho_B, \alpha)} + \frac{\mu}{\pi^2 \rho_B} (k_{F_e} + k_{F_\mu}) =: V_\mu(\rho_B, \alpha), \end{aligned} \quad (77)$$

where k_{F_e} and k_{F_μ} are respectively the Fermi momenta for electrons (e) and muons (μ). For simplicity, we here define the nuclear symmetry energy involving the isospin asymmetry, α , as

$$\begin{aligned} E_{\text{sym}}(\rho_B, \alpha) &= \frac{1}{2} \frac{\partial^2 E_B(\rho_B, \alpha)}{\partial \alpha^2} \\ &= \frac{1}{2} \frac{\partial E_{\text{ISB}}(\rho_B, \alpha)}{\partial \alpha}. \end{aligned} \quad (78)$$

Note that we explicitly keep α to consider the stability of nuclear and neutron star matter, though the nuclear symmetry energy is in general calculated at $\rho_p = \rho_n$, namely $\alpha = 0$, as shown in Eq. (22). Hence the stability constraint on chemical potential, $V_\mu(\rho_B, \alpha) > 0$, can be satisfied by assuming that $E_{\text{sym}}(\rho_B, \alpha)$ is positive at any ρ_B .

As for the pressure stability, the differentiation of $P(v, q)$ ($= P(\rho_B, \alpha)$) reads

$$- \left(\frac{\partial P}{\partial v} \right)_\mu = \rho_B^2 \left[\left(\frac{\partial P_B}{\partial \rho_B} \right)_\mu + \left(\frac{\partial P_L}{\partial \rho_B} \right)_\mu \right], \quad (79)$$

with the baryon and lepton contributions. Similar to Eq. (77), the baryon contribution is given by

$$\left(\frac{\partial P_B}{\partial \rho_B}\right)_\mu = 2\rho_B \frac{\partial E_B(\rho_B, \alpha)}{\partial \rho_B} + \rho_B^2 \frac{\partial^2 E_B(\rho_B, \alpha)}{\partial^2 \rho_B} - \rho_B^2 \left[\frac{\partial^2 E_B(\rho_B, \alpha)}{\partial \rho_B \partial \alpha} \right]^2 \bigg/ \frac{\partial^2 E_B(\rho_B, \alpha)}{\partial^2 \alpha}. \quad (80)$$

Using the thermodynamic definitions of pressure and incompressibility of infinite nuclear matter in Eqs. (28) and (29), this equation can be simplified as

$$\left(\frac{\partial P_B}{\partial \rho_B}\right)_\mu = 2 \frac{P_B(\rho_B, \alpha)}{\rho_B} + \frac{1}{9} K_B(\rho_B, \alpha) - \frac{1}{18} \frac{L_{\text{ISB}}^2(\rho_B, \alpha)}{E_{\text{sym}}(\rho_B, \alpha)}, \quad (81)$$

where the slope of ISB energy, $L_{\text{ISB}}(\rho_B, \alpha)$, is defined as

$$L_{\text{ISB}}(\rho_B, \alpha) = 3\rho_B \frac{\partial E_{\text{ISB}}(\rho_B, \alpha)}{\partial \rho_B}. \quad (82)$$

The lepton contribution is also given by the simple form under the β equilibrium condition:

$$\left(\frac{\partial P_L}{\partial \rho_B}\right)_\mu = \frac{\rho_e k_{F_e}^2 + \rho_\mu k_{F_\mu}^2}{3\mu\rho_B}. \quad (83)$$

Therefore, the stability of neutron star matter under the charge neutrality and β equilibrium conditions can be clarified by the thermodynamic constraints on chemical potential and pressure, namely $V_\mu(\rho_B, \alpha) > 0$ and

$$V_P(\rho_B, \alpha) := \left(\frac{\partial P_B}{\partial \rho_B}\right)_\mu + \left(\frac{\partial P_L}{\partial \rho_B}\right)_\mu > 0. \quad (84)$$

The thermodynamic stability is used in several calculations of nuclear and neutron star matter, for instance, the compressibility of β -equilibrated matter (Zabari et al., 2019; Kubis et al., 2020) and the phase transition between the crust and core regions in neutron stars (Routray et al., 2016; Zhang et al., 2018; Xie and Li, 2019).

3 RESULTS AND DISCUSSIONS

3.1 Nuclear models

We adopt the recently developed effective interactions labeled as the OMEG family, which are constructed to reproduce the characteristics of finite nuclei, nuclear matter, and neutron stars (Miyatsu et al., 2022a, 2023). In particular, the δ - N coupling and σ - δ mixing in the OMEG family are determined so as to support the astrophysical constraints on the neutron-star radii from the NICER mission (Miller et al., 2019, 2021; Riley et al., 2019, 2021) and the tidal deformabilities from the binary merger events due to GW signals (Abbott et al., 2018, 2020). Various theoretical calculations using the well-calibrated parameter sets based on the RMF models are also presented: BigApple (Fattoyev et al., 2020), DINO (Reed et al., 2024), FSU- δ (Li et al., 2022), FSUGarnet (Chen and Piekarewicz, 2015), FSUGold (Fattoyev and Piekarewicz, 2010), FSUGold2 (Chen and Piekarewicz, 2014), Bayesian refinement of FSUGarnet and FSUGold2, FSUGarnet+R and FSUGold2+R (Salinas and Piekarewicz, 2023a,b), HPNL0 and HPNL5 (Kumar et al., 2023), IOPB-I (Kumar et al., 2018), IU-FSU (Fattoyev et al., 2010), NL3 (Lalazissis et al., 1997),

Table 1. Model parameters for various effective interactions. The nucleon and δ -meson masses in free space are fixed at $M_N = 939$ MeV and $m_\delta = 980$ MeV. For the HPNL0 and HPNL5, we set $m_\delta = 983$ MeV (Kumar et al., 2023). The M_N is taken as $M_N = 938$ MeV only for the TM1 (Sugahara and Toki, 1994).

Models	m_σ (MeV)	m_ω (MeV)	m_ρ (MeV)	g_σ^2	g_ω^2	g_δ^2	g_ρ^2	g_2 (fm ⁻¹)	g_3	c_3	$\Lambda_{\sigma\delta}$	$\Lambda_{\omega\rho}$
OMEG0	496.500	782.660	775.260	89.384	142.847	37.699	51.744	9.976	-21.469	-	87.000	102.612
OMEG1	497.825	782.660	775.260	99.645	166.268	30.000	44.591	7.824	-1.115	100.000	95.000	75.677
OMEG2	497.820	782.660	775.260	99.641	166.269	20.000	44.364	7.823	-1.113	100.000	85.000	288.859
OMEG3	498.015	782.660	775.260	99.713	166.272	15.000	57.550	7.827	-1.105	100.000	70.000	909.825
BigApple	492.730	782.500	763.000	93.507	151.684	-	50.139	11.944	-31.832	2.684	-	1449.033
DINOa	490.050	782.500	763.000	93.942	154.443	278.788	201.454	11.501	-20.139	59.626	-	205.236
DINOb	485.795	782.500	763.000	91.032	150.806	313.178	219.270	11.651	-20.561	56.870	-	185.311
DINOc	484.162	782.500	763.000	90.648	151.032	335.813	230.653	11.642	-20.517	57.039	-	171.604
FSU- $\delta 6.2$	491.500	782.500	763.000	104.332	180.507	38.440	48.867	8.090	5.881	172.150	107.650	91.639
FSU- $\delta 6.7$	491.500	782.500	763.000	104.332	180.507	44.890	52.843	8.090	5.881	172.150	90.157	102.004
FSUGarnet	496.939	782.500	763.000	110.350	187.693	-	47.966	9.565	-7.122	137.981	-	1555.729
FSUGarnet+R	495.633	782.500	763.000	109.045	186.307	-	35.654	9.407	-6.452	138.011	-	1016.385
FSUGold	491.500	782.500	763.000	112.204	204.556	-	34.629	4.277	49.858	418.394	-	850.374
FSUGold2	497.479	782.500	763.000	108.070	183.733	-	20.145	8.546	-1.021	144.122	-	12.289
FSUGold2+R	501.611	782.500	763.000	103.793	169.483	-	32.090	10.150	-19.026	55.970	-	687.024
HPNL0	501.825	782.500	770.000	109.108	180.637	1.443	26.967	9.393	-3.405	134.110	-	267.522
HPNL5	500.972	782.500	770.000	103.502	169.568	8.903	39.724	9.270	-2.866	120.751	46.077	511.487
IOPB-I	500.000	782.500	762.500	107.971	178.268	-	30.955	10.517	-15.146	91.108	-	528.819
IU-FSU	491.500	782.500	763.000	99.427	169.835	-	46.172	8.497	0.462	144.219	-	1442.856
NL3	508.194	782.501	763.000	104.408	165.562	-	19.883	10.454	-28.955	-	-	-
PD15	480.025	780.000	763.000	97.535	173.792	22.782	60.551	7.662	6.551	169.689	-	627.406
TAMUC-FSUa	502.200	782.500	763.000	106.504	176.178	-	24.339	8.830	-6.317	103.462	-	213.858
TM1	511.198	783.000	770.000	100.580	159.111	-	21.459	7.249	0.610	71.308	-	-

Table 2. Properties of symmetric nuclear matter at ρ_0 for various effective interactions. Here, E_0 denotes the binding energy per nucleon. The bulk properties are given by coefficients in the power-series expansion of isospin-asymmetric nuclear EoS around ρ_0 in Sec. 2.4. The K_{asy} , $K_{\text{sat},2}$, and K_N are respectively expressed as $K_{\text{asy}} = K_{\text{sym}} - 6L$, $K_{\text{sat},2}(= K_\tau) = K_{\text{asy}} - J_0L/K_0$, and $K_N = K_{\text{sym}} + K_0$ (Sotani and Ota, 2022; Lattimer, 2023).

Models	ρ_0 (fm ⁻³)	M_N^*/M_N	E_0 (MeV)	K_0 (MeV)	J_0 (MeV)	E_{sym} (MeV)	L (MeV)	K_{sym} (MeV)	J_{sym} (MeV)	K_{asy} (MeV)	$K_{\text{sat},2}$ (MeV)	K_N (MeV)
OMEG0	0.1500	0.640	-16.45	280.00	-66.98	34.55	50.00	-384.43	-533.44	-684.43	-672.47	-104.43
OMEG1	0.1484	0.620	-16.38	256.00	-300.62	35.06	70.00	-218.83	-68.94	-638.83	-556.62	37.17
OMEG2	0.1484	0.620	-16.38	256.00	-300.56	33.00	45.00	-216.72	1020.63	-486.72	-433.89	39.28
OMEG3	0.1484	0.620	-16.38	256.00	-300.28	30.00	20.00	-65.85	1449.98	-185.85	-162.39	190.15
BigApple	0.155	0.609	-16.34	226.08	-209.66	31.32	40.00	89.76	1121.88	-150.21	-113.12	315.84
DINOa	0.1522	0.626	-16.16	210.00	-365.42	31.42	50.00	504.96	9316.53	204.96	291.97	714.96
DINOb	0.1525	0.632	-16.21	207.00	-412.46	33.07	70.00	608.70	9692.85	188.70	328.18	815.70
DINOc	0.1519	0.632	-16.22	206.00	-421.37	34.58	90.00	715.40	9846.87	175.40	359.49	921.40
FSU- $\delta 6.2$	0.148	0.610	-16.31	229.20	-322.12	32.53	48.21	-311.61	-92.61	-600.87	-533.12	-82.4
FSU- $\delta 6.7$	0.148	0.610	-16.31	229.20	-322.12	32.75	53.50	-227.23	673.54	-548.23	-473.04	1.97
FSUGarnet	0.153	0.579	-16.23	229.63	8.47	30.92	50.96	58.31	149.10	-247.45	-249.33	287.94
FSUGarnet+R	0.1527	0.582	-16.18	228.77	-24.37	30.89	55.79	20.00	417.64	-314.74	-308.80	248.77
FSUGold	0.1484	0.610	-16.30	230.00	-523.39	32.59	60.50	-51.27	424.15	-414.27	-276.59	178.73
FSUGold2	0.1505	0.593	-16.28	238.00	-149.49	37.62	112.80	25.21	-165.75	-651.59	-580.74	263.21
FSUGold2+R	0.1522	0.594	-16.22	241.22	-36.17	32.03	57.20	-6.89	971.30	-350.09	-341.51	234.33
HPNL0	0.1477	0.603	-16.10	227.38	-217.51	34.63	78.38	-69.89	488.76	-540.18	-465.20	157.48
HPNL5	0.1486	0.618	-16.18	230.32	-320.74	33.04	52.29	-83.86	1178.98	-397.60	-324.78	146.46
IOPB-I	0.149	0.594	-16.11	222.33	-109.15	33.36	63.70	-38.98	873.02	-421.18	-389.00	183.35
IU-FSU	0.1547	0.609	-16.40	231.30	-289.40	31.30	47.22	28.61	370.02	-254.73	-195.64	259.91
NL3	0.1483	0.595	-16.26	271.50	201.62	37.28	118.18	101.01	181.90	-608.09	-695.86	372.51
PD15	0.1484	0.618	-16.62	229.49	-399.42	35.29	42.60	-56.52	1582.27	-312.10	-237.96	172.97
TAMUC-FSUa	0.149	0.601	-16.23	245.31	-159.85	35.05	82.71	-68.69	382.54	-564.96	-511.07	176.62
TM1	0.145	0.635	-16.23	280.39	-286.69	36.84	110.60	33.50	-65.26	-630.08	-517.00	313.89

PD15 (Liliani et al., 2021), TAMUC-FSUa (Fattoyev and Piekarewicz, 2013; Piekarewicz, 2014), and TM1 (Sugahara and Toki, 1994). In Tables 1 and 2, we summarize the model parameters and the properties of symmetric nuclear matter at ρ_0 for the effective interactions used in the present study.

Table 3. Model parameters and nuclear properties for the extended version of the FSUGarnet, TAMUC-FSUa, and FSUGold2 models. For each series, the parameter c_3 is fixed by the original value shown in Table. 1.

Models	m_σ (MeV)	g_σ^2	g_ω^2	g_δ^2	g_ρ^2	g_2 (fm ⁻¹)	g_3	$\Lambda_{\omega\rho}$	E_0 (MeV)	E_{sym} (MeV)	K_{sym} (MeV)
FSUGarnet series ($L = 50.96$ MeV)											
$\delta 000$	496.94	110.35	187.69	0.00	47.97	9.56	-7.12	1555.73	-16.23	30.92	58.31
$\delta 050$	496.23	110.06	187.68	50.00	64.41	9.54	-7.11	364.29	-16.25	32.54	39.53
$\delta 100$	496.26	110.07	187.68	100.00	95.83	9.54	-7.11	290.10	-16.24	32.50	162.95
$\delta 150$	496.41	110.12	187.69	150.00	128.83	9.54	-7.10	274.42	-16.24	32.22	337.44
$\delta 200$	496.51	110.16	187.69	200.00	163.34	9.54	-7.10	276.62	-16.23	31.98	548.39
$\delta 250$	496.10	109.99	187.69	250.00	199.38	9.53	-7.10	286.98	-16.24	31.85	790.04
$\delta 300$	493.90	109.10	187.65	300.00	238.62	9.45	-7.07	303.57	-16.30	32.60	1054.19
TAMUC-FSUa series ($L = 82.71$ MeV)											
$\delta 000$	502.20	106.50	176.18	0.00	24.40	8.83	-6.32	213.86	-16.23	35.05	-68.69
$\delta 050$	502.85	106.74	176.19	50.00	53.83	8.84	-6.30	158.60	-16.21	34.55	3.69
$\delta 100$	502.75	106.70	176.19	100.00	85.18	8.83	-6.30	159.75	-16.21	34.55	104.58
$\delta 150$	502.75	106.70	176.19	150.00	117.17	8.83	-6.30	168.70	-16.21	34.50	233.64
$\delta 200$	502.75	106.70	176.19	200.00	149.71	8.83	-6.29	180.42	-16.21	34.35	389.08
$\delta 250$	502.70	106.68	176.19	250.00	182.90	8.83	-6.28	193.75	-16.20	34.15	568.48
$\delta 300$	502.10	106.44	176.19	300.00	217.36	8.81	-6.28	208.75	-16.22	34.20	767.29
FSUGold2 series ($L = 112.80$ MeV)											
$\delta 000$	497.48	108.07	183.73	0.00	20.15	8.55	-1.02	12.29	-16.28	37.62	25.21
$\delta 050$	498.00	108.28	183.74	50.00	50.47	8.56	-1.00	77.62	-16.27	37.55	87.38
$\delta 100$	497.96	108.26	183.74	100.00	81.86	8.56	-1.00	109.82	-16.27	37.51	187.87
$\delta 150$	499.99	108.27	183.74	150.00	113.85	8.56	-1.00	133.90	-16.27	37.34	320.60
$\delta 200$	498.03	108.29	183.74	200.00	146.62	8.56	-1.00	155.39	-16.27	37.12	481.08
$\delta 250$	498.09	108.31	183.74	250.00	179.93	8.56	-0.99	175.51	-16.26	36.73	668.45
$\delta 300$	497.60	108.12	183.74	300.00	214.65	8.54	-1.01	196.02	-16.27	36.59	876.59

Table 4. Model parameters and several properties for the FSUGold2 with the δ - N coupling and the quartic self-interaction of ρ meson. We set $c_3 = 144.12$ and $g_\delta^2 = 300.00$.

Models	m_σ (MeV)	g_σ^2	g_ω^2	g_ρ^2	g_2 (fm ⁻¹)	g_3	e_3	$\Lambda_{\omega\rho}$	E_0 (MeV)	E_{sym} (MeV)	K_{sym} (MeV)
$\rho 000$	497.60	108.12	183.74	214.65	8.54	-1.01	0.00	196.02	-16.27	36.59	876.59
$\rho 100$	497.60	108.11	183.74	214.97	8.54	-1.01	100.00	196.39	-16.27	36.75	875.10
$\rho 200$	497.62	108.12	183.74	215.17	8.55	-1.01	200.00	196.61	-16.27	36.85	874.16
$\rho 300$	497.64	108.13	183.74	215.39	8.55	-1.01	300.00	196.86	-16.27	36.96	873.14
$\rho 400$	497.65	108.13	183.74	215.73	8.55	-1.01	400.00	197.24	-16.27	37.13	871.55
$\rho 500$	497.71	108.16	183.74	215.95	8.55	-1.01	500.00	197.49	-16.27	37.24	870.53
$\rho 600$	497.83	108.20	183.74	216.11	8.55	-1.00	600.00	197.67	-16.27	37.32	869.79
$\rho 700$	497.79	108.19	183.74	216.51	8.55	-1.00	700.00	198.12	-16.27	37.52	867.93
$\rho 800$	497.83	108.21	183.74	216.91	8.55	-1.00	800.00	198.57	-16.27	37.72	866.08

In addition, we present the extended interactions based on the FSUGarnet, TAMUC-FSUa, and FSUGold2 models, in which the δ - N coupling are introduced to investigate the effect of δ meson. The δ - N coupling constant, g_δ , is here fixed so as to maintain the result of L from the original models, while the other parameters are readjusted to reproduce as much as possible the other characteristics, such as the binding energy per nucleon and charge radius of several closed-shell nuclei, and the saturation properties of nuclear matter. The resultant coupling constants and nuclear properties for the FSUGarnet, TAMUC-FSUa, and FSUGold2 series are listed in Table 3. Furthermore, the parameter sets for the FSUGold2 with the δ - N

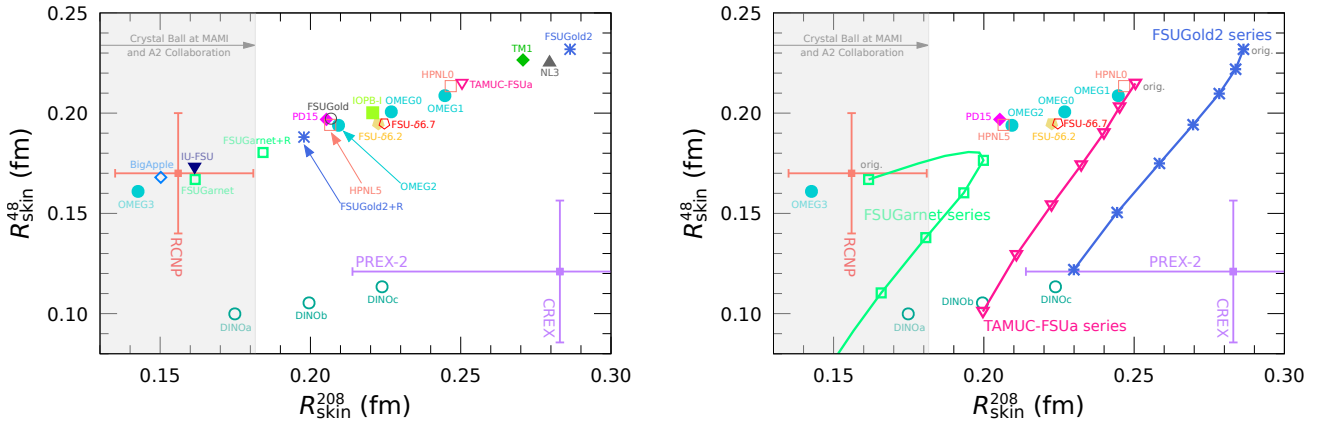


Figure 1. Neutron skin thickness of ^{40}Ca and ^{208}Pb , R_{skin}^{48} and R_{skin}^{208} . The left panel shows the results from the effective interactions presented in Tables 1 and 2. The right panel is for the FSUGarnet, TAMUC-FSUa, and FSUGold2 series in Table 3.

coupling and the quartic self-interaction of ρ meson are also given in Table 4, where the quartic coupling constant, e_3 , is varied in the range of $0 \leq e_3 \leq 800$ with the fixed parameters, $c_3 = 144.12$ and $g_\delta^2 = 300$.

3.2 Finite nuclei

The theoretical predictions for the neutron skin thickness of ^{40}Ca and ^{208}Pb , R_{skin}^{48} and R_{skin}^{208} , in the RMF models are presented in Fig. 1, compared with the experimental data: the electric dipole polarizability of ^{48}Ca (RCNP; $R_{\text{skin}}^{48} = 0.14\text{--}0.20$ fm) (Birkhan et al., 2017), the complete electric dipole response on ^{208}Pb (RCNP; $R_{\text{skin}}^{208} = 0.156^{+0.025}_{-0.021}$ fm) (Tamii et al., 2011), the coherent pion photoproduction cross sections measurement of ^{208}Pb (MAMI; $R_{\text{skin}}^{208} = 0.15 \pm 0.03(\text{stat.})^{+0.01}_{-0.03}(\text{sys.})$ fm) (Tarbert et al., 2014), and the parity-violating electron scattering off ^{48}Ca (CREX; $R_{\text{skin}}^{48} = 0.121 \pm 0.026(\text{exp.}) \pm 0.024(\text{model})$ fm) (Adhikari et al., 2022) and off ^{208}Pb (PREX-2; $R_{\text{skin}}^{208} = 0.283 \pm 0.071$ fm) (Adhikari et al., 2021).

As for the OMEG family, the OMEG0 and OMEG1 give the large values, $R_{\text{skin}}^{208} = 0.227$ fm and $R_{\text{skin}}^{208} = 0.245$ fm respectively, which meet the PREX-2 result. The OMEG2 is selected so as to match the predicted result, $R_{\text{skin}}^{208} = 0.19 \pm 0.02$ fm, by the assessment of the theoretical uncertainty on parity-violating asymmetry in ^{208}Pb (Reinhard et al., 2021). Meanwhile, the OMEG3 exhibits the small value, $R_{\text{skin}}^{48} = 0.161$ fm, which satisfies the experimental result in RCNP and is near the range of CREX experiment, $R_{\text{skin}}^{48} = 0.121 \pm 0.035$ fm. We summarize the predictions for the charge radius, R_{ch} , neutron skin thickness, R_{skin} , and weak radius, R_{wk} , of ^{48}Ca and ^{208}Pb in Table 5. We here consider the zero-point energy correction taken from the conventional Skyrme Hartree–Fock calculations (Reinhard et al., 1986; Sugahara and Toki, 1994). The R_{ch} is defined as

$$R_{\text{ch}} = \sqrt{R_p^2 + (0.8783)^2}, \quad (85)$$

with R_p being the point proton radius (Chen and Piekarewicz, 2014).

We see the linear correlation between R_{skin}^{48} and R_{skin}^{208} in the left panel of Fig. 1. In general, the larger R_{skin}^{48} and R_{skin}^{208} are obtained by the models with the larger L (see Table 2). To explain the results from RCNP, L should be small such as the OMEG3, BigApple, FSUGarnet, and IU-FSU. In contrast, the DINO

Table 5. Predictions for the charge radius, R_{ch} , neutron skin thickness, R_{skin} , weak radius, R_{wk} , and weak skin thickness, $R_{\text{wk}} - R_{\text{ch}}$, of ^{48}Ca and ^{208}Pb in fm. The PREX-2 and CREX results are also presented (Adhikari et al., 2021, 2022).

Models	^{48}Ca				^{208}Pb			
	R_{ch}	R_{skin}	R_{wk}	$R_{\text{wk}} - R_{\text{ch}}$	R_{ch}	R_{skin}	R_{wk}	$R_{\text{wk}} - R_{\text{ch}}$
OMEG0	3.499	0.201	3.689	0.189	5.514	0.227	5.738	0.223
OMEG1	3.495	0.209	3.693	0.198	5.532	0.245	5.774	0.242
OMEG2	3.500	0.194	3.682	0.183	5.536	0.209	5.741	0.205
OMEG3	3.510	0.161	3.659	0.149	5.549	0.143	5.685	0.136
BigApple	3.496	0.168	3.652	0.156	5.513	0.150	5.657	0.144
DIN0a	3.510	0.100	3.597	0.086	5.531	0.175	5.700	0.169
DIN0b	3.514	0.105	3.606	0.092	5.531	0.200	5.726	0.195
DIN0c	3.519	0.113	3.619	0.100	5.532	0.224	5.752	0.220
FSU- δ 6.2	3.501	0.195	3.685	0.183	5.547	0.223	5.766	0.219
FSU- δ 6.7	3.502	0.195	3.685	0.184	5.549	0.225	5.770	0.221
FSUGarnet	3.471	0.167	3.626	0.155	5.514	0.162	5.670	0.156
FSUGarnet+R	3.473	0.180	3.643	0.168	5.513	0.184	5.692	0.179
FSUGold	3.479	0.197	3.664	0.186	5.540	0.207	5.742	0.203
FSUGold2	3.469	0.232	3.690	0.221	5.512	0.286	5.797	0.285
FSUGold2+R	3.478	0.188	3.654	0.176	5.509	0.198	5.702	0.193
HPNL0	3.490	0.213	3.692	0.203	5.551	0.247	5.795	0.244
HPNL5	3.493	0.194	3.676	0.183	5.545	0.207	5.747	0.202
IOPB-I	3.493	0.200	3.682	0.189	5.548	0.221	5.765	0.217
IU-FSU	3.473	0.173	3.634	0.161	5.501	0.161	5.656	0.156
NL3	3.490	0.226	3.705	0.215	5.529	0.280	5.807	0.278
PD15	3.520	0.197	3.706	0.186	5.561	0.205	5.762	0.201
TAMUC-FSUa	3.483	0.215	3.687	0.204	5.528	0.250	5.776	0.248
TM1	3.499	0.227	3.715	0.216	5.556	0.271	5.825	0.269
FSUGarnet series								
δ 000	3.471	0.167	3.626	0.155	5.514	0.162	5.670	0.156
δ 050	3.466	0.176	3.630	0.164	5.496	0.200	5.691	0.195
δ 100	3.469	0.160	3.616	0.148	5.497	0.193	5.685	0.188
δ 150	3.472	0.138	3.597	0.125	5.480	0.181	5.675	0.175
δ 200	3.477	0.110	3.573	0.097	5.504	0.166	5.664	0.160
δ 250	3.481	0.078	3.544	0.063	5.508	0.151	5.652	0.144
δ 300	3.470	0.050	3.505	0.035	5.509	0.142	5.645	0.136
TAMUC-FSUa series								
δ 000	3.483	0.215	3.687	0.204	5.528	0.250	5.776	0.248
δ 050	3.484	0.203	3.676	0.192	5.528	0.245	5.770	0.242
δ 100	3.487	0.190	3.666	0.179	5.529	0.240	5.765	0.237
δ 150	3.491	0.174	3.653	0.162	5.530	0.232	5.759	0.229
δ 200	3.495	0.154	3.637	0.142	5.532	0.223	5.751	0.219
δ 250	3.501	0.129	3.617	0.116	5.536	0.211	5.742	0.207
δ 300	3.506	0.101	3.593	0.087	5.538	0.200	5.734	0.195
FSUGold2 series								
δ 000	3.469	0.232	3.690	0.221	5.512	0.286	5.797	0.285
δ 050	3.470	0.222	3.681	0.211	5.511	0.284	5.793	0.282
δ 100	3.473	0.210	3.672	0.199	5.511	0.278	5.788	0.277
δ 150	3.477	0.194	3.660	0.183	5.513	0.270	5.781	0.268
δ 200	3.482	0.175	3.645	0.163	5.516	0.258	5.772	0.256
δ 250	3.487	0.150	3.625	0.138	5.521	0.244	5.762	0.241
δ 300	3.494	0.123	3.603	0.109	5.525	0.230	5.753	0.226
Experiment	3.477	0.121	3.636	0.159	5.501	0.283	5.800	0.299

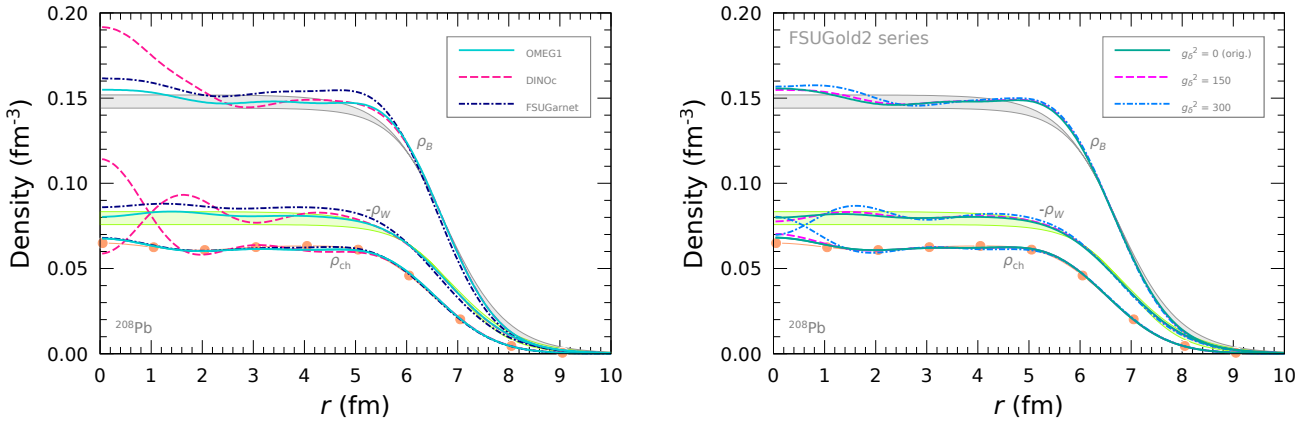


Figure 2. Baryon, charge, and weak charge densities, ρ_B , ρ_{ch} , and ρ_W , for ^{208}Pb . The density profiles for the OMEG1, DINOc, and FSUGarnet are given in the left panel. The right panel is for the FSUGold2 series.

family is located far from the points calculated by the other RMF models. As explained in Reed et al. (2024), the DINO family expresses the large K_{sym} by means of the huge δ - N and ρ - N couplings. Although it is difficult to support the PREX-2 and CREX results simultaneously, only the DINOc successfully aligns with both data sets.

To clarify the effect of δ meson on the characteristics of finite nuclei, we describe the correlation between R_{skin}^{48} and R_{skin}^{208} for the FSUGarnet, TAMUC-FSUa, and FSUGold2 series in the right panel of Fig. 1. We also display the calculations based on the other RMF models including the δ meson as well as the σ , ω , and ρ mesons. As shown in Table 3, K_{sym} becomes large as g_δ^2 increases. Consequently, the TAMUC-FSUa, and FSUGold2 series draw the lines from the upper right to the bottom left. In particular, the FSUGold2 with the large δ - N coupling ($g_\delta^2 \geq 250$) supports both experimental data from the parity-violating electron scattering. On the other hand, the FSUGarnet series moves away from the PREX-2 and CREX results when the large g_δ^2 is introduced.

The density profiles in ^{208}Pb are displayed in Fig. 2. We here present the baryon, charge, and weak charge densities, ρ_B ($= \rho_p + \rho_n$), ρ_{ch} , and ρ_W , with the experimental results (Adhikari et al., 2021; De Vries et al., 1987). The ρ_W is approximately expressed as

$$\rho_W(\mathbf{r}) \simeq Q_p \rho_{ch}(\mathbf{r}) + Q_n \int d\mathbf{r}' G_p^E(|\mathbf{r} - \mathbf{r}'|) \rho_n(\mathbf{r}), \quad (86)$$

with $Q_{p(n)}$ being the proton (neutron) weak charge and G_p^E being the proton electric form factor (Horowitz et al., 2001, 2012; Niksic et al., 2002). The OMEG family is calibrated so as to reproduce $-\rho_W$ and ρ_B in ^{208}Pb by the PREX-2 experiment.

In the left panel of Fig. 2, we present the density profiles for the OMEG1, DINOc, FSUGarnet. The OMEG1 and FSUGarnet adequately satisfy the density distributions of ρ_{ch} from the elastic electron scattering (De Vries et al., 1987). On the other hand, the DINOc possesses the instability around the core of nuclei because of the strong δ - N coupling constant (Reed et al., 2024). As a result, the density profiles, ρ_B , ρ_{ch} , and ρ_W , show the large density fluctuations around the core.

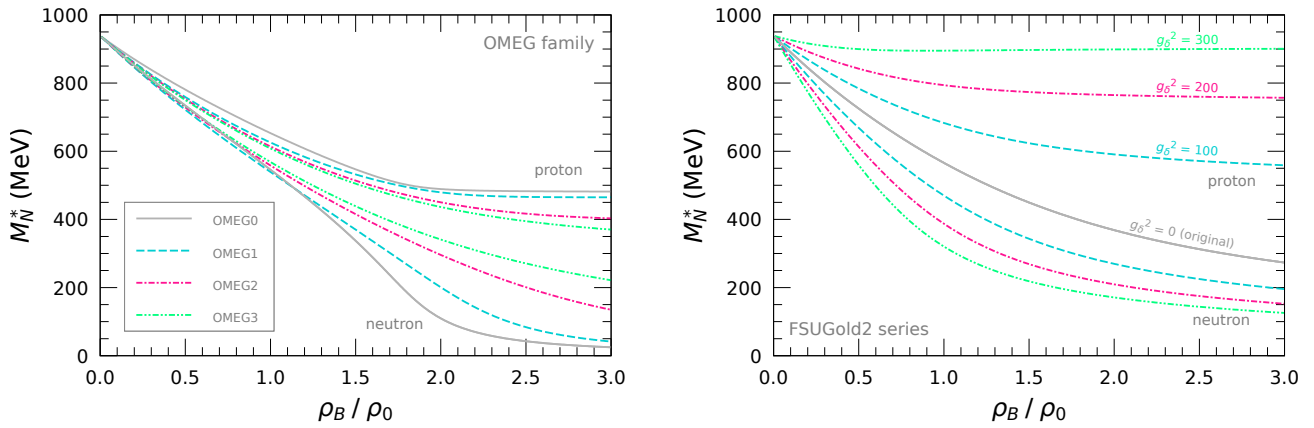


Figure 3. Effective nucleon mass, M_N^* , as a function of ρ_B / ρ_0 for the OMEG family (left panel) and the FSUGold2 series (right panel).

The effect of δ - N coupling on the density profiles for the FSUGold2 series is illustrated in the right panel of Fig. 2. There is almost no difference up to $g_\delta^2 = 150$. In the case of $g_\delta^2 = 300$, ρ_{ch} and ρ_W begin to show the instability around the core, but ρ_B still matches the experimental data from PREX-2 (Adhikari et al., 2021). When the larger value, $g_\delta^2 > 300$, is taken, the unexpectedly large fluctuations of ρ_{ch} and ρ_W emerge around the core, and the wave functions do not converge numerically. In the present study, we thus impose the limit on the δ - N coupling as $g_\delta^2 \leq 300$ for the FSUGold2 series. We here comment that this defect can not be solved even if one considers the quartic self-interactions of δ and/or ρ mesons in Eq. (2), which less affect R_{skin}^{48} and R_{skin}^{208} .

3.3 Infinite nuclear matter

The δ -meson effect can be clearly seen in the effective nucleon mass, M_N^* , in Eq. (3). Displayed in Fig. 3 is the density dependence of M_N^* in pure neutron matter for the OMEG family and the FSUGold2 series. When the ρ meson only is included, the RMF model gives the equal effective mass of proton and neutron. However, the iso-scalar δ meson is responsible for the mass splitting between protons and neutrons, where M_p^* is much heavier than M_n^* at high densities. Compared with the OMEG family, the FSUGold2 series shows the strong mass splitting, as g_δ^2 increases, even at low densities. It is implied that the neutron distribution is more spread out than the proton one, because M_n^* is lighter, and then, the large fluctuations of ρ_{ch} and ρ_W appear around the core of ^{208}Pb as shown in Fig 2. Due to the δ - N coupling and the σ - δ mixing, M_p^* and M_n^* respectively reach the almost constant values at high densities in all the cases.

The density dependence of nuclear symmetry energy, E_{sym} , in Eq. (57) is depicted in Fig. 4. We here present the calculations using the OMEG, FSU- δ , and DINO families. Furthermore, we use the conventional ones (the NL3, FSUGold2, TAMUC-FSUa, IOPB-I, and FSUGarnet models). In addition, several experimental or theoretical constraints are presented. Figure 4 highlights significant differences in E_{sym} at high densities, that is, whereas the conventional calculations show a monotonic increase in E_{sym} , the models with the δ meson exhibit more complex behavior. In particular, the DINO family predicts a large E_{sym} above $1.5\rho_0$ as the δ meson amplifies E_{sym} in dense nuclear matter (Miyatsu et al., 2022b). The OMEG and FSU- δ families, on the other hand, display unusual E_{sym} trends depending on the strength of δ - N coupling and σ - δ mixing. The σ - δ mixing has a weak influence on E_{sym} below ρ_0 , but, as discussed by Zabari et al. (2019), it becomes substantial above ρ_0 . Specifically, the σ - δ mixing reduces E_{sym} at

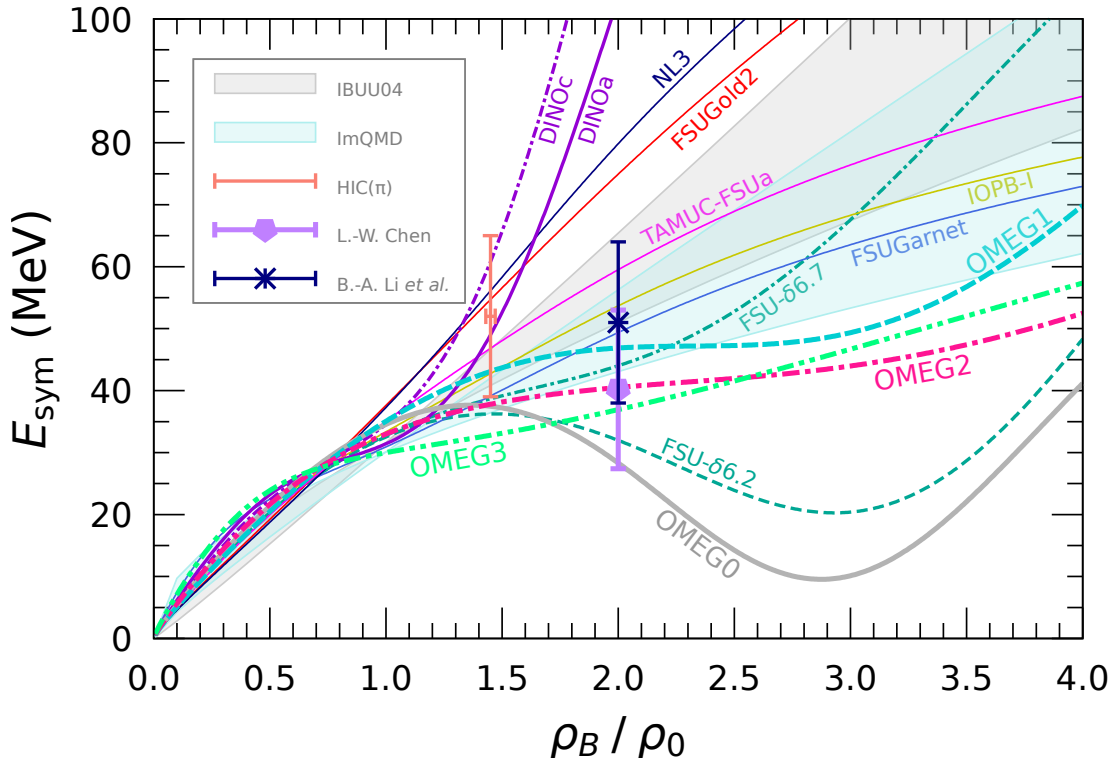


Figure 4. Density dependence of nuclear symmetry energy, E_{sym} . The shaded regions are the results from analyses of HIC data using the isospin-dependent Boltzmann-Uehling-Uhlenbeck (IBUU04) and improved quantum molecular dynamics (ImQMD) transport models (Chen et al., 2005a; Li and Chen, 2005; Tsang et al., 2009). The recent experimental constraint from the pion emission in heavy-ion reactions is expressed as HIC(π) with $E_{\text{sym}}(\rho_B) = 52 \pm 13$ MeV at $\rho_B/\rho_0 = 1.45 \pm 0.2$ (Estee et al., 2021; Lynch and Tsang, 2022; Tsang et al., 2024). We also present two theoretical constraints on the magnitude of E_{sym} at $2\rho_0$ with $E_{\text{sym}}(2\rho_0) \simeq 40.2 \pm 12.8$ MeV by Chen (2015) and $E_{\text{sym}}(2\rho_0) \simeq 51 \pm 13$ MeV by Li et al. (2021).

high densities, partially offsetting the increase from the δ - N interaction. Furthermore, in the OMEG0 and FSU- $\delta 6.2$, the inflection points appear above ρ_0 and the dip emerges around $2.5\rho_0$ – $3.5\rho_0$. This behavior is similar to the cusp in E_{sym} in the skyrmion crystal approach (Ma and Rho, 2021; Lee et al., 2022) and to the results from the Skyrme Hartree-Fock calculations (Chen et al., 2005b). We note that, as explained in Sec. 2.5, the thermodynamic constraint on chemical potential in isospin-asymmetric nuclear matter, $V_\mu(\rho_B, \alpha) > 0$, is satisfied over all densities, namely $E_{\text{sym}}(\rho_B, \alpha) > E_{\text{sym}}(\rho_B) > 0$.

Based on the Lorentz decomposition of nucleon self-energy in Sec.2.4, E_{sym} is generally divided into the kinetic and potential terms, $E_{\text{sym}}^{\text{kin}}$ and $E_{\text{sym}}^{\text{pot}}$, as $E_{\text{sym}} = E_{\text{sym}}^{\text{kin}} + E_{\text{sym}}^{\text{pot}}$. In RMF approximation, only the isovector mesons contribute to $E_{\text{sym}}^{\text{pot}}$ as $E_{\text{sym}}^{\text{pot}} = E_{\text{sym}}^s + E_{\text{sym}}^0$, where the scalar (s) and time (0) components, E_{sym}^s and E_{sym}^0 , are respectively given by the δ and ρ mesons. We show the Lorentz decomposition of E_{sym} for the OMEG family and the FSUGold2 series as a function of ρ_B/ρ_0 in Fig. 5. The top panels are the density dependence of E_{sym} and $E_{\text{sym}}^{\text{kin}}$. We see that the unique behavior of E_{sym} in the OMEG family is caused by $E_{\text{sym}}^{\text{pot}}$ because $E_{\text{sym}}^{\text{kin}}$ is almost the same as in both cases. The contents of $E_{\text{sym}}^{\text{pot}}$ are given in the middle and bottom panels of Fig. 5. It is found that E_{sym}^s is negative while E_{sym}^0 is positive, which is similar to the general understanding of N - N interaction described by the nuclear attractive and repulsive

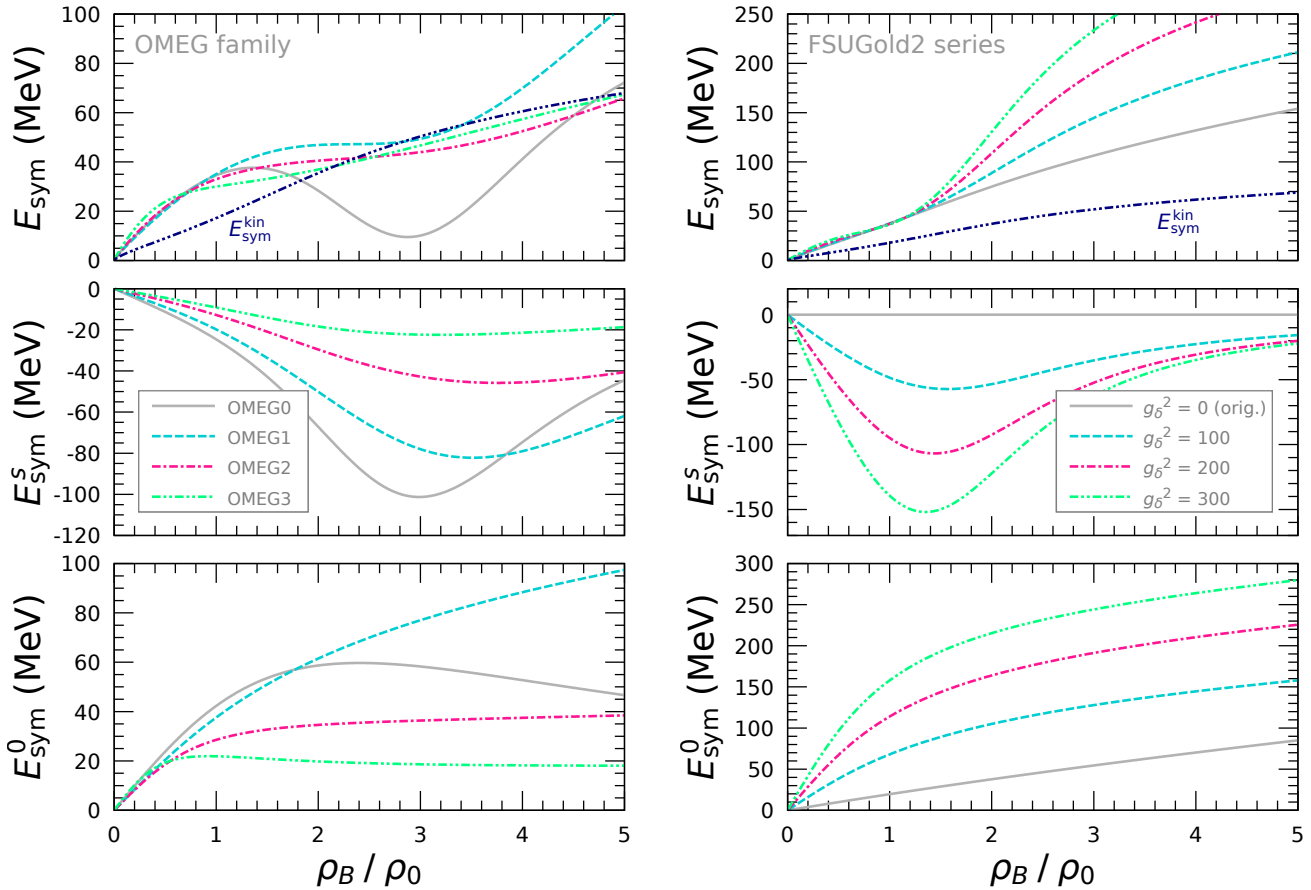


Figure 5. Lorentz decomposition of nuclear symmetry energy, E_{sym} , for the OMEG family (left panels) and the FSUGold2 series (right panels). The total E_{sym} and the kinetic term, $E_{\text{sym}}^{\text{kin}}$, are presented in the top panels. The scalar (time) component of potential term, E_{sym}^s (E_{sym}^0), is given in the middle (bottom) panels.

forces. It is noticeable that, for the FSUGold2 series, E_{sym}^s is strongly influenced by the δ - N coupling above ρ_0 , and the contribution of E_{sym}^s is small at high densities. Conversely, for the OMEG family, the σ - δ mixing shows less impact on E_{sym}^s below ρ_0 , but it strongly affects E_{sym}^s at high densities. When the absolute value of E_{sym}^s is larger than that of E_{sym}^0 , $E_{\text{sym}}^{\text{pot}}$ has the rapid reduction, and then E_{sym} shows a dip around $3\rho_0$ as in the cases for the OMEG0 and FSU- δ 6.2 in Fig. 4.

The EoSs for symmetric nuclear matter and pure neutron matter are displayed in Fig. 6 with the constraints on the nuclear EoS extracted from the analyses of particle flow data in HICs (Danielewicz et al., 2002; Fuchs, 2006; Lynch et al., 2009). In both panels, we show the various EoSs calculated by the OMEG, DINO, and FSU- δ families, and the FSUGarnet and FSUGold2 models. The δ meson does not affect P in symmetric nuclear matter. All the cases except for the OMEG0 are well constructed to match the HIC data in symmetric nuclear matter because of the small K_0 . However, the stiffer EoS with $K_0 \simeq 285$ MeV is still acceptable, taking into account the recent simulation of Au+Au collisions (Oliinychenko et al., 2023). In contrast, the δ meson has a large impact on P in pure neutron matter. The DINOa and DINOc show the hard EoSs, which are far from the constraints from HICs, due to the large δ - N coupling. Meanwhile, the strong

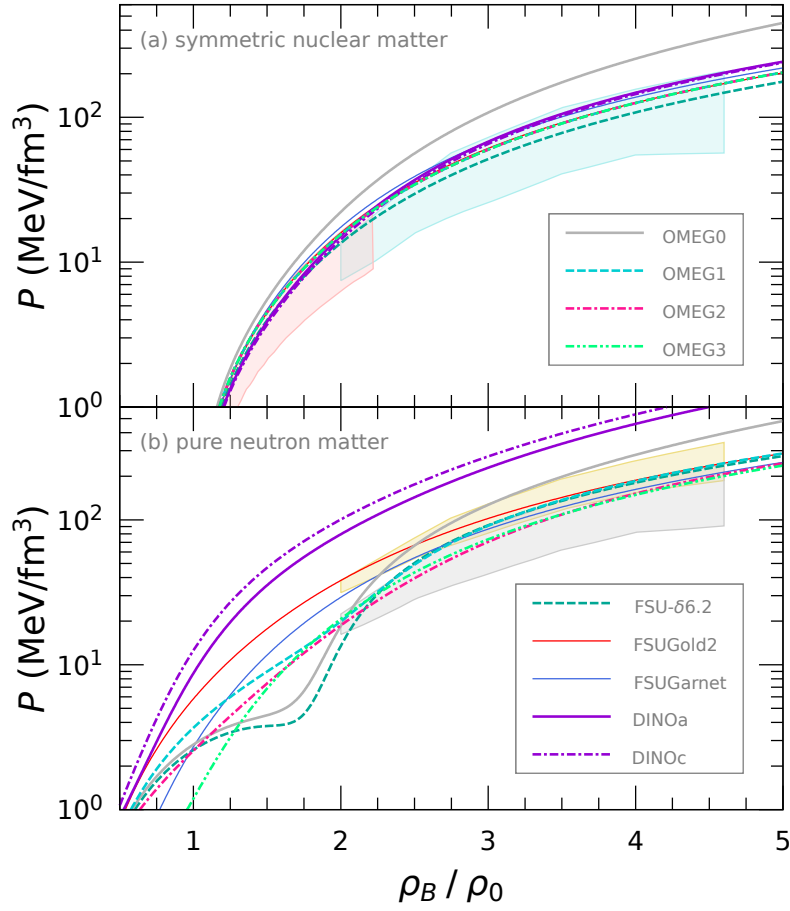


Figure 6. EoS—pressure, P , as a function of ρ_B / ρ_0 —for (a) symmetric nuclear matter and for (b) pure neutron matter. The shaded areas represent the constraints from elliptical flow data (Danielewicz et al., 2002) and kaon production data (Fuchs, 2006; Lynch et al., 2009).

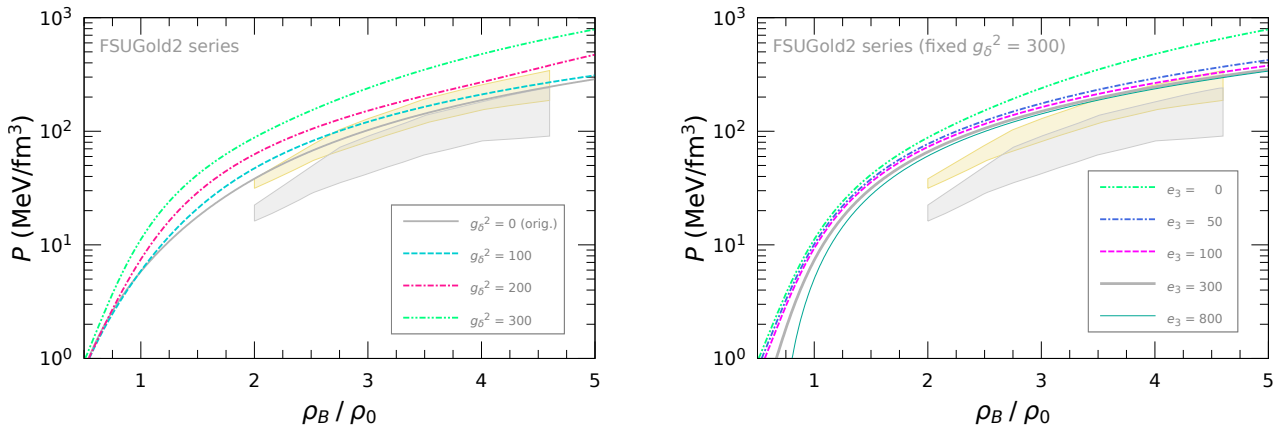


Figure 7. EoS for pure neutron matter for the FSUGold2 series. The left panel shows the dependence of δ - N coupling square, g_δ^2 . In the right panel, the influence of quartic ρ -meson self-interaction, e_3 , is presented with the fixed parameter of $g_\delta^2 = 300$ (see Table 4).

σ - δ mixing softens the EoSs extremely for the OMEG and FSU- δ families in the density region from ρ_0 to $2\rho_0$, around which the characteristics of a canonical $1.4 M_\odot$ neutron star are generally determined.

We present the EoS for pure neutron matter for the FSUGold2 series in Fig. 7. In the left panel, the EoS becomes hard with increasing the δ - N coupling, and the EoS with $g_\delta^2 = 300$ exceeds the HIC results as in the cases for the DINO family in Fig. 6. Hence, we find that, even if the large δ - N coupling is introduced simply, it is not easy to explain simultaneously both properties of dense nuclear matter and characteristics of finite nuclei for R_{skin}^{48} and R_{skin}^{208} in Fig. 1. In order to suppress such excessive stiffness of EoSs for pure neutron matter due to the δ - N coupling, we additionally include the quartic self-interaction of ρ meson in the FSUGold2 model with the upper limit of $g_\delta^2 = 300$ (see Table 4), given in the right panel of Fig. 7. The EoS is soft and again reaches the upper edge of the constraint from HICs with increasing the quartic coupling, e_3 , whose effect is almost imperceptible below ρ_0 .

3.4 Neutron star physics

In studying neutron star physics, the EoS for nonuniform matter is additionally required as well as that for uniform nuclear matter since the radius of a neutron star is remarkably sensitive to the nuclear EoS at very low densities (Glendenning, 1997). In the present study, to cover the crust region, we adopt the MYN13 EoS, in which nuclei are taken into consideration using the Thomas-Fermi calculation in nonuniform matter and the EoS for infinite nuclear matter is constructed with the relativistic Hartree-Fock calculation (Miyatsu et al., 2012; Katayama et al., 2012; Miyatsu et al., 2013b, 2015). We list in Table 6 the predicted stellar properties, which are calculated by solving the Tolman–Oppenheimer–Volkoff (TOV) equation (Tolman, 1939; Oppenheimer and Volkoff, 1939).

There are three methods used widely to determine the crust-core transition density, ρ_t (Sulaksono et al., 2014): the thermo-dynamical method, the dynamical method, and the random-phase-approximation method. We employ the first method in the present study. As explained in Sec. 2.5, the stability of nuclear and neutron star matter is determined by the constraints on chemical potential and pressure, $V_\mu(\rho_B, \alpha) > 0$ and $V_P(\rho_B, \alpha) > 0$, in the first law of thermodynamics. Since the proton fraction, Y_p , is supposed to be small in the crust region, the second-order Taylor series approximation of the nuclear EoS is generally adopted in the density derivative of baryon pressure, $(\partial P_B / \partial \rho_B)_\mu$, in Eq. (80) (Kubis, 2007). However, it has been reported that the parabolic approximation of isospin-asymmetric nuclear EoS may be misleading as regards the predictions for ρ_t (Routray et al., 2016). We thus employ the exact nuclear EoS to calculate V_P defined in Eq. (81).

We summarize the results of ρ_t in the second column of Table 6. Compared with the results from the Taylor series expansion, the our results settle between the second-order and fourth-order calculations. For example, for the FSUGold, the exact value is $\rho_t = 0.079 \text{ fm}^{-3}$ while the second-order (fourth-order) result is $\rho_t^{2\text{nd}} = 0.089$ ($\rho_t^{4\text{th}} = 0.051$) fm^{-3} (see Table 2 in Routray et al. (2016)). In addition, the current results are almost the same as the transition density from the pasta phase to the homogeneous nuclear matter in the model calculation with Thomas-Fermi approximation (Providência et al., 2014). The EoS for neutron star matter in the OMEG family is presented in Fig. 8. The crust-core phase transition occurs at $V_P = 0$, which is also described in the left panel of Fig. 9. As it is well known, the EoS with larger L gives the smaller ρ_t (Li et al., 2019).

Since the large σ - δ mixing enhances the rapid reduction of E_{sym} around $3\rho_0$ as shown in Fig. 4, we have to investigate the stability of neutron star matter. Similar to the crust-core phase transition, we adopt the thermo-dynamical method. It is especially important to apply the exact nuclear EoS to V_P because Y_p is by no means small and the Taylor series expansion is prohibited at high densities. It is found that the

Table 6. Properties of neutron stars. We calculate the crust-core transition density, ρ_t , and the observables at the canonical- and maximum-mass points.

Models	ρ_t (fm ⁻¹)	$R_{1.4}$ (km)	$\rho_{1.4}$ (fm ⁻¹)	$\Lambda_{1.4}$	M_{\max} (M_{\odot})	R_{\max} (km)	ρ_{\max} (fm ⁻¹)	Λ_{\max}
OMEG0	0.093	12.43	0.359	498	2.61	12.16	0.772	4
OMEG1	0.079	12.76	0.402	515	2.13	11.70	0.917	14
OMEG2	0.093	12.40	0.428	458	2.07	11.31	0.980	13
OMEG3	0.104	12.40	0.409	462	2.07	11.39	0.962	14
BigApple	0.096	13.03	0.329	677	2.60	12.38	0.759	5
DIN0a	0.092	14.11	0.307	1047	2.17	12.30	0.854	16
DIN0b	0.087	14.37	0.306	1136	2.15	12.26	0.870	16
DIN0c	0.083	14.63	0.301	1237	2.15	12.30	0.871	16
FSU- δ 6.2	0.083	12.08	0.409	416	2.10	11.53	0.922	16
FSU- δ 6.7	0.082	12.82	0.386	573	2.05	11.76	0.917	20
FSUGarnet	0.084	12.87	0.382	596	2.07	11.66	0.932	17
FSUGarnet+R	0.083	12.94	0.384	616	2.06	11.66	0.938	18
FSUGold	0.079	12.32	0.520	400	1.72	10.80	1.156	32
FSUGold2	0.061	14.00	0.351	873	2.07	12.09	0.904	19
FSUGold2+R	0.087	13.19	0.347	715	2.26	12.10	0.848	12
HPNL0	0.072	13.32	0.383	674	2.03	11.74	0.946	19
HPNL5	0.088	12.76	0.408	551	2.01	11.43	0.980	18
IOPB-I	0.081	13.21	0.362	693	2.15	11.92	0.890	15
IU-FSU	0.088	12.49	0.433	482	1.94	11.19	1.027	19
NL3	0.063	14.68	0.272	1255	2.77	13.30	0.668	4
PD15	0.094	12.49	0.434	488	1.92	11.19	1.026	21
TAMUC-FSUa	0.073	13.48	0.365	725	2.10	11.92	0.909	17
TM1	0.068	14.31	0.320	1038	2.18	12.37	0.852	16
FSUGarnet series								
δ 000	0.084	12.87	0.382	596	2.07	11.66	0.932	17
δ 050	0.094	13.09	0.360	681	2.10	11.91	0.893	18
δ 100	0.097	13.37	0.336	784	2.13	12.15	0.859	19
δ 150	0.097	13.62	0.318	893	2.14	12.31	0.841	20
δ 200	0.097	13.82	0.307	973	2.13	12.40	0.833	21
δ 250	0.096	13.96	0.301	1031	2.13	12.42	0.834	22
δ 300	0.095	14.02	0.300	1059	2.12	12.39	0.840	22
TAMUC-FSUa series								
δ 000	0.073	13.48	0.365	725	2.10	11.92	0.909	17
δ 050	0.076	13.72	0.338	850	2.14	12.19	0.867	17
δ 100	0.080	13.94	0.318	947	2.16	12.39	0.839	18
δ 150	0.083	14.15	0.302	1073	2.17	12.53	0.824	19
δ 200	0.085	14.33	0.292	1158	2.17	12.60	0.818	20
δ 250	0.086	14.48	0.285	1249	2.16	12.63	0.817	21
δ 300	0.086	14.58	0.283	1276	2.16	12.63	0.820	21
FSUGold2 series								
δ 000	0.061	14.00	0.351	873	2.07	12.09	0.904	19
δ 050	0.064	14.13	0.335	950	2.08	12.25	0.881	21
δ 100	0.069	14.29	0.318	1045	2.09	12.39	0.861	22
δ 150	0.074	14.45	0.304	1151	2.10	12.49	0.849	23
δ 200	0.078	14.58	0.295	1227	2.10	12.54	0.844	24
δ 250	0.080	14.68	0.289	1297	2.09	12.56	0.843	24
δ 300	0.082	14.74	0.287	1334	2.08	12.55	0.846	24

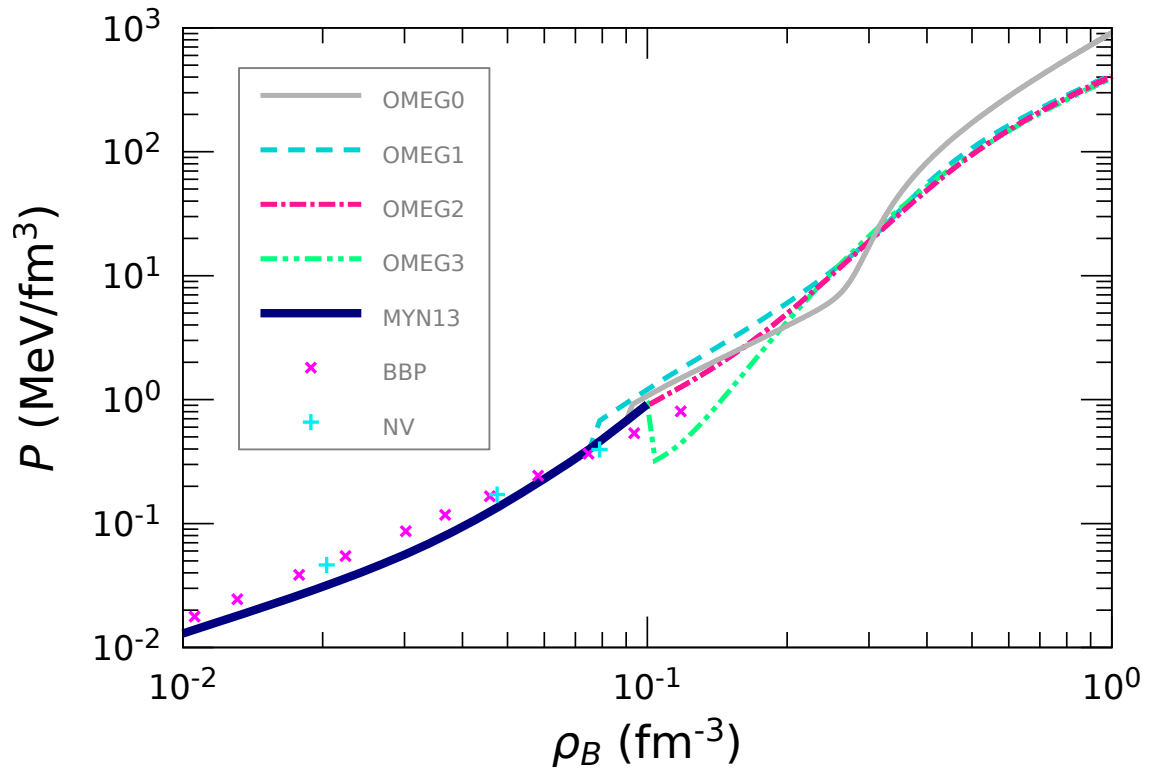


Figure 8. EoS for neutron star matter for the OMEG family. The inner-crust region is described by the EoSs of MYN13 (Miyatsu et al., 2013b), BBP (Baym et al., 1971), and NV (Negele and Vautherin, 1973).

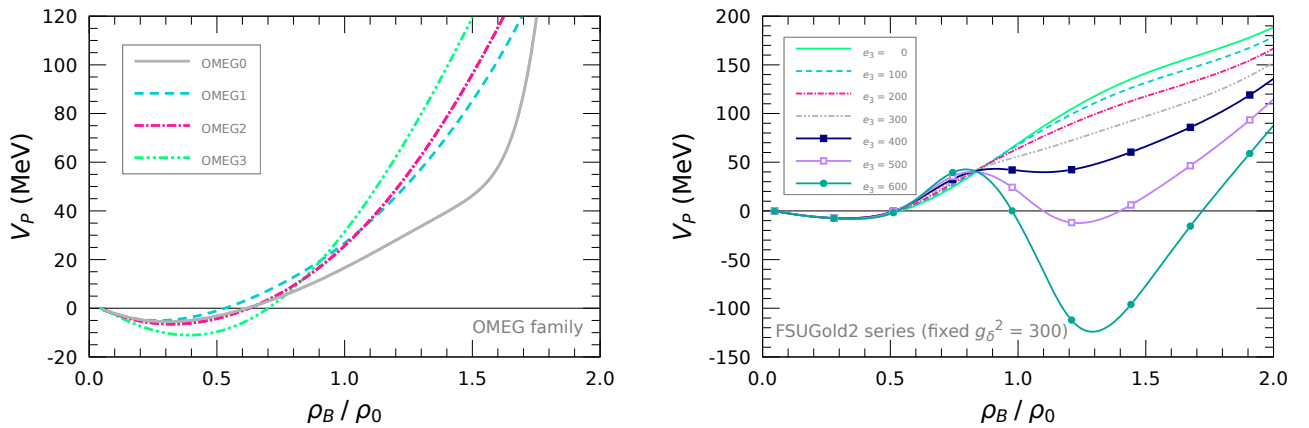


Figure 9. Thermodynamic stability of pressure, V_P , in neutron star matter for the OMEG family (left panel) and for the FSUGold2 series with the fixed parameter of $g_\delta^2 = 300$ (right panel).

constraint on chemical potential, $V_\mu > 0$, is always satisfied as E_{sym} is positive at any densities. Hence, all we have to do is check the thermodynamic stability of pressure, V_P . In Fig. 9, we show V_P in neutron star matter. In general, V_P changes from negative to positive at ρ_t , and the stable EoS possesses $V_P > 0$ even at high densities. Despite the OMEG0 give a strong concavity in E_{sym} by the σ - δ mixing, it satisfies the

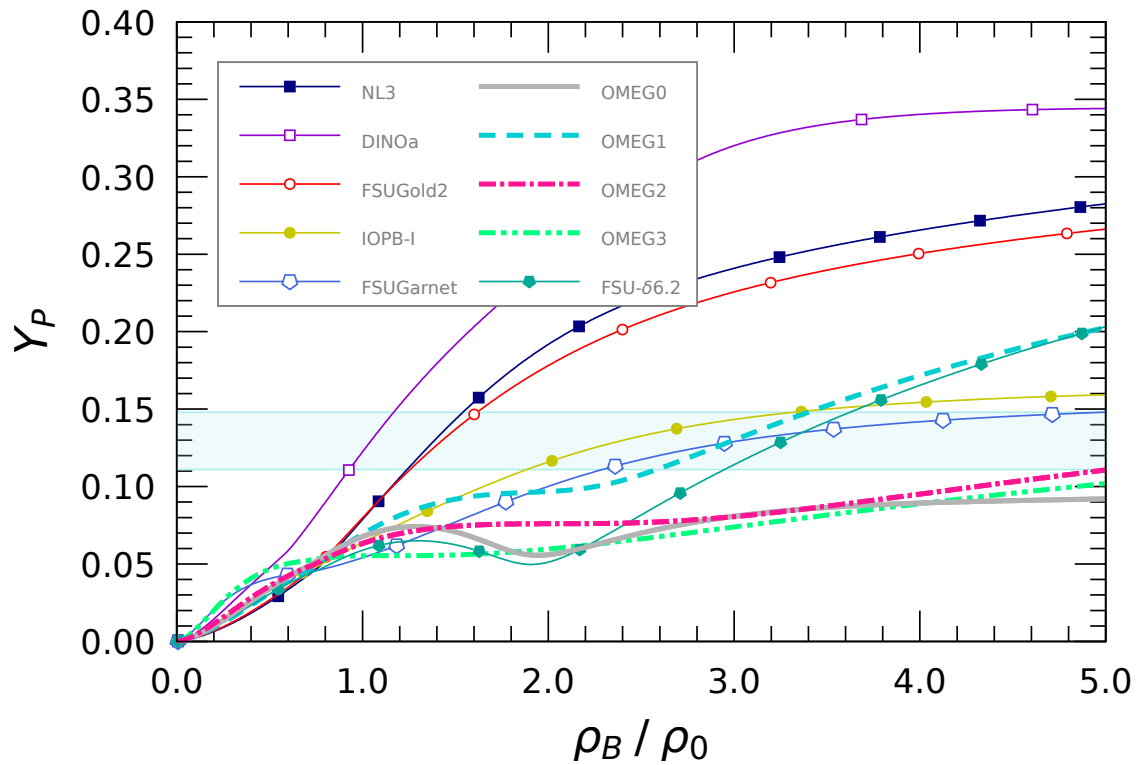


Figure 10. Proton fraction, $Y_p (= \rho_p/\rho_B)$, in neutron star matter. The shaded band is the threshold for the direct URCA process (Maruyama and Chiba, 1999; Horowitz and Piekarewicz, 2002).

thermodynamic stability. In the right panel of Fig. 9, we show V_P for the FSUGold2 series. The neutron star matter keeps $V_P > 0$ when the δ - N coupling only is included, whereas the large quartic self-interaction of ρ meson, e_3 , makes the matter unstable. Though the quartic ρ -meson self-interaction is useful to figure out the HIC data as mentioned in the right panel of Fig. 7, the large value of e_3 is unfavorable to the neutron star physics.

We illustrate in Fig. 10 the proton fraction, Y_p , in neutron star matter with the threshold for the direct URCA process. The direct URCA process is visible only when Y_p is large enough to conserve momentum in β -equilibrated matter, in which the Fermi momenta of neutrons, protons, and electron must satisfy the relation: $k_{F_n} \leq k_{F_p} + k_{F_e}$. Hence, Y_p can be estimated as $0.111 \leq Y_p \leq 0.148$, above which the direct URCA cooling occurs (Maruyama and Chiba, 1999; Horowitz and Piekarewicz, 2002; Page et al., 2006). The Y_p for the DINOa grows quickly with increasing ρ_B due to the large δ - N coupling, and then the direct URCA process is allowed sufficiently at $2\rho_0$, which corresponds to the core density of a canonical $1.4 M_\odot$ neutron star. Conversely, in the OMEG and FSU- δ families, the σ - δ mixing suppresses Y_p , and then delays the direct URCA process. Particularly, the direct URCA process never occurs for the OMEG0, OMEG2, and OMEG3 in the current density region, and thus the so-called modified URCA process, which is the standard model of neutron-star coolings, mainly takes place for the neutrino emission (Lattimer et al., 1991). Alternatively, the possibility of exotic degrees of freedom in the core of a neutron star, such as hyperons, quarks, gluons and/or some unusual condensations of boson-like matter, should be taken into account to understand the rapid neutron star cooling.

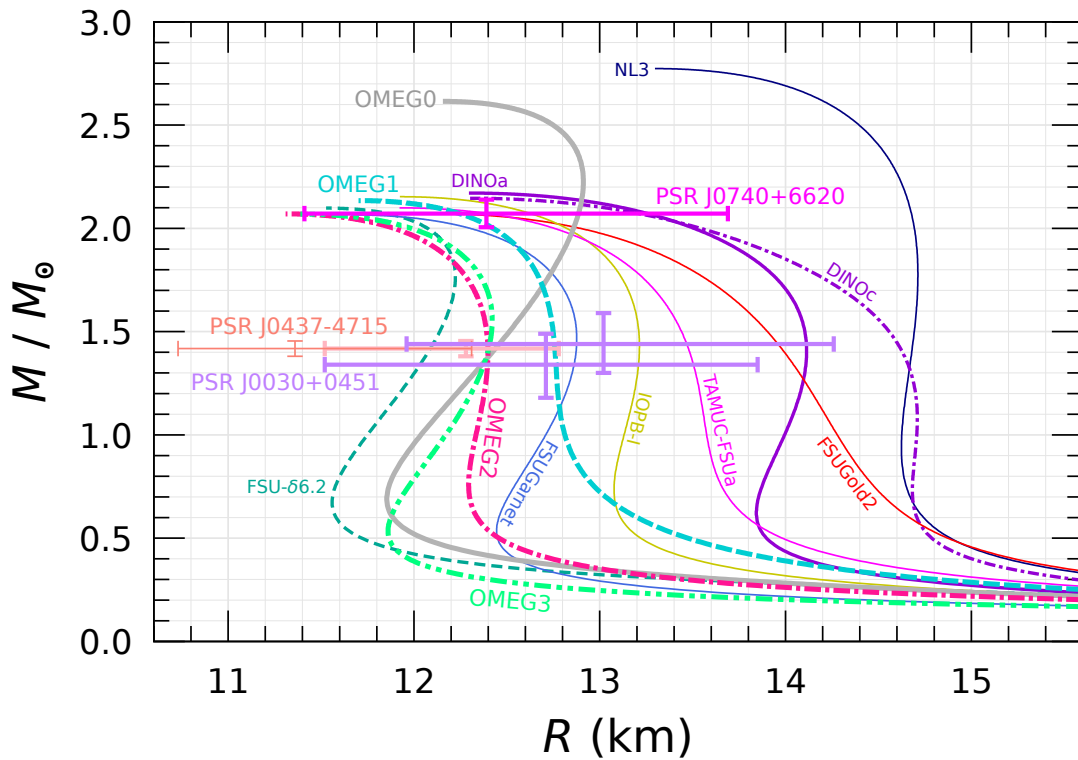


Figure 11. Mass–radius relations of neutron stars. The NICER observation data are supplemented by the constraints from PSR J0030+0451 ($1.44^{+0.15}_{-0.14} M_{\odot}$ and $13.02^{+1.24}_{-1.06}$ km, and $1.34^{+0.15}_{-0.16} M_{\odot}$ and $12.71^{+1.14}_{-1.19}$ km) (Miller et al., 2019; Riley et al., 2019), PSR J0740+6620 ($2.072^{+0.067}_{-0.066} M_{\odot}$ and $12.39^{+1.30}_{-0.98}$ km) (Cromartie et al., 2019; Fonseca et al., 2021; Riley et al., 2021), and PSR J0437–4715 ($12.28^{+0.50}_{-0.76}$ km at $1.4 M_{\odot}$, and $1.418 \pm 0.037 M_{\odot}$ and $11.36^{+0.95}_{-0.63}$ km) (Rutherford et al., 2024; Choudhury et al., 2024).

The mass(M)–radius(R) relations of neutron stars are displayed in Fig. 11. We here show the astrophysical constraints from the NICER observations: PSR J0030+0451 (Miller et al., 2019; Riley et al., 2019), PSR J0740+6620 (Cromartie et al., 2019; Fonseca et al., 2021; Riley et al., 2021), and PSR J0437–4715 (Rutherford et al., 2024; Choudhury et al., 2024). According to the observation from PSR J0740+6620, the maximum mass of a neutron star, M_{\max} , should be larger than $2M_{\odot}$. Thus the EoS involving the large R , such as the NL3, is ruled out. It is found that the large δ – N coupling affects the large R in the DINO family, whereas the σ – δ mixing makes R small in the OMEG family. In particular, though the DINOa and OMEG0 have the same L as $L = 50$ MeV, their M – R relations are completely different and the difference of R at canonical-mass point reads approximately 1.7 km (see also Table 6). The OMEG family can support not only the NICER constraint on $R_{1.4}$ from PSR J0030+0451 but also that from PSR J0437–4715, which is the latest result based on new chiral effective field theory inputs (Rutherford et al., 2024).

The dimensionless tidal deformability, Λ , of neutron stars is displayed in Fig. 12 as a function of M/M_{\odot} . The Λ is defined as $\Lambda = \frac{2}{3}k_2 (R/M)^5$ with k_2 being the second Love number (Hinderer, 2008; Hinderer et al., 2010). The astrophysical constraints on Λ at the canonical-mass point, $\Lambda_{1.4}$, from the binary merger

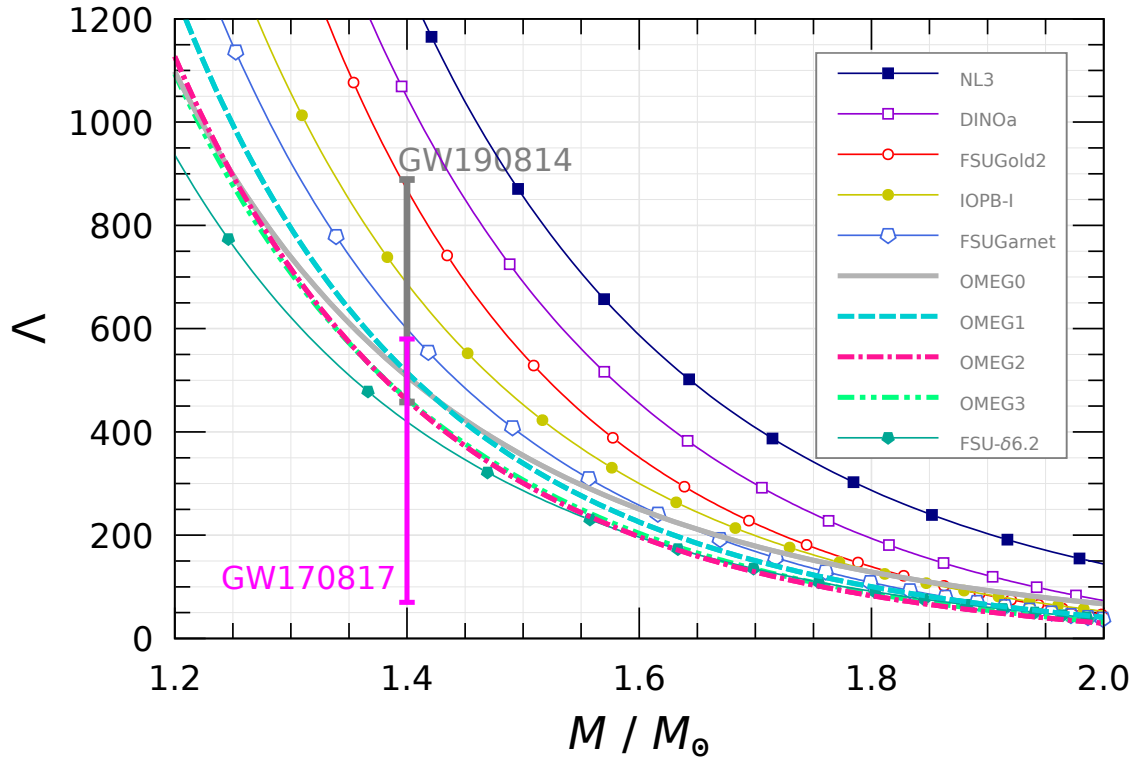


Figure 12. Dimensionless tidal deformability, Λ , of neutron stars. We present the constraints on $\Lambda_{1.4}$ from the binary merger events, GW170817 ($\Lambda_{1.4} = 190_{-120}^{+390}$) (Abbott et al., 2018) and GW190814 ($\Lambda_{1.4} = 616_{-158}^{+273}$) (Abbott et al., 2020).

events detected by the Advanced LIGO and Advanced Virgo observatories are also presented as follows: $\Lambda_{1.4} = 190_{-120}^{+390}$ for GW170817 (Abbott et al., 2018) and $\Lambda_{1.4} = 616_{-158}^{+273}$ for GW190814 (Abbott et al., 2020). As explained in Miyatsu et al. (2022b), the δ - N coupling enlarges Λ for the DINOa, and then $\Lambda_{1.4}$ lies far from the constraints on $\Lambda_{1.4}$ from GW190814. On the other hand, the σ - δ mixing has a promising effect on Λ , and thus the OMEG family sufficiently matches the severe constraints from both GW170817 and GW190814.

4 SUMMARY AND CONCLUSION

We have developed a new family of nuclear EoSs, referred to as the OMEG family, using the RMF model with nonlinear couplings between the isoscalar and isovector mesons. In addition to the σ , ω , and ρ mesons, we have also included the δ meson to examine the ground-state properties of finite, closed-shell nuclei as well as the characteristics of nuclear and neutron star matter. Specifically, we have investigated the effects of δ - N coupling and σ - δ mixing on the EoS for both nuclear and neutron star matter. The model parameters for the OMEG family have been calibrated so as to satisfy the constraints from the particle flow data in HICs (Danielewicz et al., 2002; Fuchs, 2006; Lynch et al., 2009), the observed neutron-star mass of PSR J0740+6620 (Cromartie et al., 2019; Fonseca et al., 2021; Riley et al., 2021), and the dimensionless tidal deformability, $\Lambda_{1.4}$, from the neutron star merger, GW170817 (Abbott et al., 2018), as well as the results from the PREX-2 and CREX experiments (Adhikari et al., 2021, 2022).

It has been found that the δ - N coupling and the σ - δ mixing significantly influence the properties of isospin-asymmetric nuclear matter and finite nuclei, playing a crucial role in reconciling terrestrial experiments with astrophysical observations of neutron stars. The strong δ - N coupling for the FSUGold2 series can simultaneously explain the large R_{skin}^{208} and the small R_{skin}^{48} measured by the PREX-2 and CREX experiments. However, it seems difficult that the FSUGold2 series satisfy the combined constraints from the particle flow data in HICs and astrophysical observations, such as the EoS for pure neutron matter and the Λ of neutron stars. Even with the inclusion of quartic ρ -meson self-interaction in the FSUGold2 series, both experimental and observational results can not be understood, because the large e_3 destabilizes neutron star matter. In contrast, the OMEG family can satisfy the recent measurement of $R_{1.4} = 12.28_{-0.76}^{+0.50}$ km for PSR J0437-4715 from NICER (Rutherford et al., 2024) and the stringent constraint on $\Lambda_{1.4} = 190_{-120}^{+390}$ from GW170817 (Abbott et al., 2018). This is attributed to the σ - δ mixing, which suppresses E_{sym} above $2\rho_0$, resulting in a softer nuclear EoS in the density region corresponding to the core density of the canonical neutron stars.

Finally, we comment that the further theoretical studies are necessary to reconcile the R_{skin} measured by proton (in)elastic scattering with that obtained from parity-violating electron scattering. In particular, it is very significant to investigate the discrepancy between the PREX-2 data (Adhikari et al., 2021) and the results from RCNP (Zenihiro et al., 2010; Tamii et al., 2011) and MAMI (Tarbert et al., 2014). It is also essential to consider the effect of isospin symmetry breaking on asymmetric nuclear matter from the quark level (Guichon, 1988; Saito and Thomas, 1994a,b; Saito et al., 2007, 2024; Nagai et al., 2008).

ACKNOWLEDGMENTS

T.M. would like to thank H. Sagawa and G. Colò for informative discussions of the neutron skin thickness of heavy nuclei.

FUNDING

This work was supported by the National Research Foundation of Korea (Grant Nos. RS-2023-00242196, NRF-2021R1A6A1A03043957, NRF-2020R1A2C3006177, and NRF-2018R1A5A1025563).

REFERENCES

- Abbott, B. P., Abbott, R., Abbott, T. D., et al. (2017). GW170817: Observation of Gravitational Waves from a Binary Neutron Star Inspiral. *Phys. Rev. Lett.* 119, 161101. doi:10.1103/PhysRevLett.119.161101
- Abbott, B. P., Abbott, R., Abbott, T. D., et al. (2018). GW170817: Measurements of neutron star radii and equation of state. *Phys. Rev. Lett.* 121, 161101. doi:10.1103/PhysRevLett.121.161101
- Abbott, B. P., Abbott, R., Abbott, T. D., et al. (2019). Properties of the binary neutron star merger GW170817. *Phys. Rev. X* 9, 011001. doi:10.1103/PhysRevX.9.011001
- Abbott, R., Abbott, T. D., Abraham, S., et al. (2020). GW190814: Gravitational Waves from the Coalescence of a 23 Solar Mass Black Hole with a 2.6 Solar Mass Compact Object. *Astrophys. J. Lett.* 896, L44. doi:10.3847/2041-8213/ab960f
- Adhikari, D. et al. (2021). Accurate Determination of the Neutron Skin Thickness of ^{208}Pb through Parity-Violation in Electron Scattering. *Phys. Rev. Lett.* 126, 172502. doi:10.1103/PhysRevLett.126.172502
- Adhikari, D. et al. (2022). Precision Determination of the Neutral Weak Form Factor of ^{48}Ca . *Phys. Rev. Lett.* 129, 042501. doi:10.1103/PhysRevLett.129.042501

- Alam, N., Agrawal, B. K., Fortin, M., Pais, H., Providência, C., Raduta, A. R., et al. (2016). Strong correlations of neutron star radii with the slopes of nuclear matter incompressibility and symmetry energy at saturation. *Phys. Rev. C* 94, 052801. doi:10.1103/PhysRevC.94.052801
- Alford, M. G., Brodie, L., Haber, A., and Tews, I. (2022). Relativistic mean-field theories for neutron-star physics based on chiral effective field theory. *Phys. Rev. C* 106, 055804. doi:10.1103/PhysRevC.106.055804
- Annala, E., Gorda, T., Kurkela, A., and Vuorinen, A. (2018). Gravitational-wave constraints on the neutron-star-matter Equation of State. *Phys. Rev. Lett.* 120, 172703. doi:10.1103/PhysRevLett.120.172703
- Arzoumanian, Z., Brazier, A., Burke-Spolaor, S., et al. (2018). The NANOGrav 11-year Data Set: High-precision timing of 45 Millisecond Pulsars. *Astrophys. J. Suppl.* 235, 37. doi:10.3847/1538-4365/aab5b0
- Baym, G., Bethe, H. A., and Pethick, C. (1971). Neutron star matter. *Nucl. Phys. A* 175, 225–271. doi:10.1016/0375-9474(71)90281-8
- Bethe, H. A., Brown, G. E., Applegate, J., and Lattimer, J. M. (1979). Equation of state in the gravitational collapse of stars. *Nucl. Phys. A* 324, 487–533. doi:10.1016/0375-9474(79)90596-7
- Birkhan, J. et al. (2017). Electric dipole polarizability of ^{48}Ca and implications for the neutron skin. *Phys. Rev. Lett.* 118, 252501. doi:10.1103/PhysRevLett.118.252501
- Boguta, J. and Bodmer, A. R. (1977). Relativistic Calculation of Nuclear Matter and the Nuclear Surface. *Nucl. Phys. A* 292, 413–428. doi:10.1016/0375-9474(77)90626-1
- Cai, B.-J. and Chen, L.-W. (2012). Lorentz covariant nucleon self-energy decomposition of the nuclear symmetry energy. *Phys. Lett. B* 711, 104–108. doi:10.1016/j.physletb.2012.03.058
- Chen, L.-W. (2015). Symmetry energy systematics and its high density behavior. *EPJ Web Conf.* 88, 00017. doi:10.1051/epjconf/20158800017
- Chen, L.-W., Cai, B.-J., Ko, C. M., Li, B.-A., Shen, C., and Xu, J. (2009). High-order effects on the incompressibility of isospin asymmetric nuclear matter. *Phys. Rev. C* 80, 014322. doi:10.1103/PhysRevC.80.014322
- Chen, L.-W., Ko, C. M., and Li, B.-A. (2005a). Determination of the stiffness of the nuclear symmetry energy from isospin diffusion. *Phys. Rev. Lett.* 94, 032701. doi:10.1103/PhysRevLett.94.032701
- Chen, L.-W., Ko, C. M., and Li, B.-A. (2005b). Nuclear matter symmetry energy and the neutron skin thickness of heavy nuclei. *Phys. Rev. C* 72, 064309. doi:10.1103/PhysRevC.72.064309
- Chen, L.-W., Ko, C. M., and Li, B.-A. (2007). Isospin-dependent properties of asymmetric nuclear matter in relativistic mean-field models. *Phys. Rev. C* 76, 054316. doi:10.1103/PhysRevC.76.054316
- Chen, W.-C. and Piekarewicz, J. (2014). Building relativistic mean field models for finite nuclei and neutron stars. *Phys. Rev. C* 90, 044305. doi:10.1103/PhysRevC.90.044305
- Chen, W.-C. and Piekarewicz, J. (2015). Searching for isovector signatures in the neutron-rich oxygen and calcium isotopes. *Phys. Lett. B* 748, 284–288. doi:10.1016/j.physletb.2015.07.020
- Choudhury, D. et al. (2024). A NICER View of the Nearest and Brightest Millisecond Pulsar: PSR J0437–4715. *Astrophys. J. Lett.* 971, L20. doi:10.3847/2041-8213/ad5a6f
- Cromartie, H. T. et al. (2019). Relativistic Shapiro delay measurements of an extremely massive millisecond pulsar. *Nature Astron.* 4, 72–76. doi:10.1038/s41550-019-0880-2
- Czerski, P., De Pace, A., and Molinari, A. (2002). Revisiting the Hugenholtz-Van Hove theorem in nuclear matter. *Phys. Rev. C* 65, 044317. doi:10.1103/PhysRevC.65.044317
- Danielewicz, P., Lacey, R., and Lynch, W. G. (2002). Determination of the equation of state of dense matter. *Science* 298, 1592–1596. doi:10.1126/science.1078070

- De Vries, H., De Jager, C. W., and De Vries, C. (1987). Nuclear charge and magnetization density distribution parameters from elastic electron scattering. *Atom. Data Nucl. Data Tabl.* 36, 495–536. doi:10.1016/0092-640X(87)90013-1
- Demorest, P., Pennucci, T., Ransom, S., Roberts, M., and Hessels, J. (2010). Shapiro Delay Measurement of A Two Solar Mass Neutron Star. *Nature* 467, 1081–1083. doi:10.1038/nature09466
- Estee, J. et al. (2021). Probing the Symmetry Energy with the Spectral Pion Ratio. *Phys. Rev. Lett.* 126, 162701. doi:10.1103/PhysRevLett.126.162701
- Fattoyev, F. J., Horowitz, C. J., Piekarewicz, J., and Reed, B. (2020). GW190814: Impact of a 2.6 solar mass neutron star on the nucleonic equations of state. *Phys. Rev. C* 102, 065805. doi:10.1103/PhysRevC.102.065805
- Fattoyev, F. J., Horowitz, C. J., Piekarewicz, J., and Shen, G. (2010). Relativistic effective interaction for nuclei, giant resonances, and neutron stars. *Phys. Rev. C* 82, 055803. doi:10.1103/PhysRevC.82.055803
- Fattoyev, F. J. and Piekarewicz, J. (2010). Sensitivity of the Moment of Inertia of Neutron Stars to the Equation of State of Neutron-Rich Matter. *Phys. Rev. C* 82, 025810. doi:10.1103/PhysRevC.82.025810
- Fattoyev, F. J. and Piekarewicz, J. (2013). Has a thick neutron skin in ^{208}Pb been ruled out? *Phys. Rev. Lett.* 111, 162501. doi:10.1103/PhysRevLett.111.162501
- Fonseca, E. et al. (2021). Refined Mass and Geometric Measurements of the High-mass PSR J0740+6620. *Astrophys. J. Lett.* 915, L12. doi:10.3847/2041-8213/ac03b8
- Fuchs, C. (2006). Kaon production in heavy ion reactions at intermediate energies. *Prog. Part. Nucl. Phys.* 56, 1–103. doi:10.1016/j.pnpnp.2005.07.004
- Glendenning, N. K. (1997). *Compact stars: Nuclear physics, particle physics, and general relativity*
- Glendenning, N. K. and Moszkowski, S. A. (1991). Reconciliation of neutron star masses and binding of the lambda in hypernuclei. *Phys. Rev. Lett.* 67, 2414–2417. doi:10.1103/PhysRevLett.67.2414
- Guichon, P. A. M. (1988). A Possible Quark Mechanism for the Saturation of Nuclear Matter. *Phys. Lett. B* 200, 235–240. doi:10.1016/0370-2693(88)90762-9
- Haidari, M. M. and Sharma, M. M. (2008). Sigma-omega meson coupling and properties of nuclei and nuclear matter. *Nucl. Phys. A* 803, 159–172. doi:10.1016/j.nuclphysa.2008.02.296
- Hinderer, T. (2008). Tidal Love numbers of neutron stars. *Astrophys. J.* 677, 1216–1220. doi:10.1086/533487. [Erratum: *Astrophys. J.* 697, 964 (2009)]
- Hinderer, T., Lackey, B. D., Lang, R. N., and Read, J. S. (2010). Tidal deformability of neutron stars with realistic equations of state and their gravitational wave signatures in binary inspiral. *Phys. Rev. D* 81, 123016. doi:10.1103/PhysRevD.81.123016
- Horowitz, C. J. and Piekarewicz, J. (2001a). Neutron star structure and the neutron radius of Pb-208. *Phys. Rev. Lett.* 86, 5647. doi:10.1103/PhysRevLett.86.5647
- Horowitz, C. J. and Piekarewicz, J. (2001b). The Neutron radii of Pb-208 and neutron stars. *Phys. Rev. C* 64, 062802. doi:10.1103/PhysRevC.64.062802
- Horowitz, C. J. and Piekarewicz, J. (2002). Constraining URCA cooling of neutron stars from the neutron radius of Pb-208. *Phys. Rev. C* 66, 055803. doi:10.1103/PhysRevC.66.055803
- Horowitz, C. J., Pollock, S. J., Souder, P. A., and Michaels, R. (2001). Parity violating measurements of neutron densities. *Phys. Rev. C* 63, 025501. doi:10.1103/PhysRevC.63.025501
- Horowitz, C. J. et al. (2012). Weak charge form factor and radius of ^{208}Pb through parity violation in electron scattering. *Phys. Rev. C* 85, 032501. doi:10.1103/PhysRevC.85.032501
- Hu, J., Bao, S., Zhang, Y., Nakazato, K., Sumiyoshi, K., and Shen, H. (2020). Effects of symmetry energy on the radius and tidal deformability of neutron stars in the relativistic mean-field model. *PTEP* 2020, 043D01. doi:10.1093/ptep/ptaa016

- Katayama, T., Miyatsu, T., and Saito, K. (2012). EoS for massive neutron stars. *Astrophys. J. Suppl.* 203, 22. doi:10.1088/0067-0049/203/2/22
- Kubis, S. (2007). The nuclear symmetry energy and stability of matter in neutron star. *Phys. Rev. C* 76, 025801. doi:10.1103/PhysRevC.76.025801
- Kubis, S., Wójcik, W., Castillo, D. A., and Zabari, N. (2023). Relativistic mean-field model for the ultracompact low-mass neutron star HESS J1731-347. *Phys. Rev. C* 108, 045803. doi:10.1103/PhysRevC.108.045803
- Kubis, S., Wójcik, W., and Zabari, N. (2020). Multilayer neutron stars with scalar mesons crossing term. *Phys. Rev. C* 102, 065803. doi:10.1103/PhysRevC.102.065803
- Kumar, B., Agrawal, B. K., and Patra, S. K. (2018). New relativistic effective interaction for finite nuclei, infinite nuclear matter and neutron stars. *Phys. Rev. C* 97, 045806. doi:10.1103/PhysRevC.97.045806
- Kumar, S., Kumar, M., Kumar, R., and Dhiman, S. K. (2023). Implications of isoscalar and isovector scalar meson mixed interaction on nuclear and neutron star properties. *Phys. Rev. C* 108, 055802. doi:10.1103/PhysRevC.108.055802
- Lalazissis, G. A., König, J., and Ring, P. (1997). A New parametrization for the Lagrangian density of relativistic mean field theory. *Phys. Rev. C* 55, 540–543. doi:10.1103/PhysRevC.55.540
- Lattimer, J. M. (2014). Symmetry energy in nuclei and neutron stars. *Nucl. Phys. A* 928, 276–295. doi:10.1016/j.nuclphysa.2014.04.008
- Lattimer, J. M. (2023). Constraints on Nuclear Symmetry Energy Parameters. *Particles* 6, 30–56. doi:10.3390/particles6010003
- Lattimer, J. M. and Prakash, M. (2007). Neutron Star Observations: Prognosis for Equation of State Constraints. *Phys. Rept.* 442, 109–165. doi:10.1016/j.physrep.2007.02.003
- Lattimer, J. M., Prakash, M., Pethick, C. J., and Haensel, P. (1991). Direct URCA process in neutron stars. *Phys. Rev. Lett.* 66, 2701–2704. doi:10.1103/PhysRevLett.66.2701
- Lattimer, J. M. and Swesty, F. D. (1991). A Generalized equation of state for hot, dense matter. *Nucl. Phys. A* 535, 331–376. doi:10.1016/0375-9474(91)90452-C
- Lee, H. K., Ma, Y.-L., Paeng, W.-G., and Rho, M. (2022). Cusp in the symmetry energy, speed of sound in neutron stars and emergent pseudo-conformal symmetry. *Mod. Phys. Lett. A* 37, 2230003. doi:10.1142/S0217732322300038
- Li, B.-A., Cai, B.-J., Xie, W.-J., and Zhang, N.-B. (2021). Progress in Constraining Nuclear Symmetry Energy Using Neutron Star Observables Since GW170817. *Universe* 7, 182. doi:10.3390/universe7060182
- Li, B.-A. and Chen, L.-W. (2005). Nucleon-nucleon cross sections in neutron-rich matter and isospin transport in heavy-ion reactions at intermediate energies. *Phys. Rev. C* 72, 064611. doi:10.1103/PhysRevC.72.064611
- Li, B.-A., Chen, L.-W., and Ko, C. M. (2008). Recent Progress and New Challenges in Isospin Physics with Heavy-Ion Reactions. *Phys. Rept.* 464, 113–281. doi:10.1016/j.physrep.2008.04.005
- Li, B.-A., Krastev, P. G., Wen, D.-H., and Zhang, N.-B. (2019). Towards Understanding Astrophysical Effects of Nuclear Symmetry Energy. *Eur. Phys. J. A* 55, 117. doi:10.1140/epja/i2019-12780-8
- Li, B.-A. and Magno, M. (2020). Curvature-slope correlation of nuclear symmetry energy and its imprints on the crust-core transition, radius and tidal deformability of canonical neutron stars. *Phys. Rev. C* 102, 045807. doi:10.1103/PhysRevC.102.045807
- Li, F., Cai, B.-J., Zhou, Y., Jiang, W.-Z., and Chen, L.-W. (2022). Effects of Isoscalar- and Isovector-scalar Meson Mixing on Neutron Star Structure. *Astrophys. J.* 929, 183. doi:10.3847/1538-4357/ac5e2a

- Liliani, N., Dinningrum, J. P., and Sulaksono, A. (2021). Tensor and Coulomb-exchange terms in the relativistic mean-field model with δ -meson and isoscalar-isovector coupling. *Phys. Rev. C* 104, 015804. doi:10.1103/PhysRevC.104.015804
- Lim, Y. and Holt, J. W. (2018). Neutron star tidal deformabilities constrained by nuclear theory and experiment. *Phys. Rev. Lett.* 121, 062701. doi:10.1103/PhysRevLett.121.062701
- Lim, Y. and Schwenk, A. (2024). Symmetry energy and neutron star properties constrained by chiral effective field theory calculations. *Phys. Rev. C* 109, 035801. doi:10.1103/PhysRevC.109.035801
- Lopes, L. L. (2024). Role of the symmetry energy slope in neutron stars: Exploring the model dependency. *Phys. Rev. C* 110, 015805. doi:10.1103/PhysRevC.110.015805
- Lynch, W. G. and Tsang, M. B. (2022). Decoding the density dependence of the nuclear symmetry energy. *Phys. Lett. B* 830, 137098. doi:10.1016/j.physletb.2022.137098
- Lynch, W. G., Tsang, M. B., Zhang, Y., Danielewicz, P., Famiano, M., Li, Z., et al. (2009). Probing the Symmetry Energy with Heavy Ions. *Prog. Part. Nucl. Phys.* 62, 427. doi:10.1016/j.pnpnp.2009.01.001
- Ma, Y.-L. and Rho, M. (2021). Topology change, emergent symmetries and compact star matter. *AAPPS Bull.* 31, 16. doi:10.1007/s43673-021-00016-1
- Machleidt, R. (1989). The Meson theory of nuclear forces and nuclear structure. *Adv. Nucl. Phys.* 19, 189–376
- Machleidt, R., Holinde, K., and Elster, C. (1987). The Bonn Meson Exchange Model for the Nucleon Nucleon Interaction. *Phys. Rept.* 149, 1–89. doi:10.1016/S0370-1573(87)80002-9
- Malik, T., Dexheimer, V., and Providência, C. (2024). Astrophysics and nuclear physics informed interactions in dense matter: Inclusion of PSR J0437-4715. *Phys. Rev. D* 110, 043042. doi:10.1103/PhysRevD.110.043042
- Maruyama, T. and Chiba, S. (1999). Equation of state of neutron star matter and the isovector nucleon optical model potential. *J. Phys. G* 25, 2361–2369. doi:10.1088/0954-3899/25/12/306
- Miller, M. C., Lamb, F. K., Dittmann, A. J., et al. (2021). The Radius of PSR J0740+6620 from NICER and XMM-Newton Data. *Astrophys. J. Lett.* 918, L28. doi:10.3847/2041-8213/ac089b
- Miller, M. C. et al. (2019). PSR J0030+0451 Mass and Radius from *NICER* Data and Implications for the Properties of Neutron Star Matter. *Astrophys. J. Lett.* 887, L24. doi:10.3847/2041-8213/ab50c5
- Miyatsu, T., Cheoun, M.-K., Ishizuka, C., Kim, K. S., Maruyama, T., and Saito, K. (2020). Decomposition of nuclear symmetry energy based on Lorentz-covariant nucleon self-energies in relativistic Hartree-Fock approximation. *Phys. Lett. B* 803, 135282. doi:10.1016/j.physletb.2020.135282
- Miyatsu, T., Cheoun, M.-K., Kim, K., and Saito, K. (2022a). Massive neutron stars with small radii in relativistic mean-field models optimized to nuclear ground states. *Preprint arXiv:2209.02861 [nucl-th]*. doi:10.48550/arXiv.2209.02861
- Miyatsu, T., Cheoun, M.-K., Kim, K., and Saito, K. (2023). Can the PREX-2 and CREX results be understood by relativistic mean-field models with the astrophysical constraints? *Phys. Lett. B* 843, 138013. doi:10.1016/j.physletb.2023.138013
- Miyatsu, T., Cheoun, M.-K., and Saito, K. (2013a). Equation of state for neutron stars in SU(3) flavor symmetry. *Phys. Rev. C* 88, 015802. doi:10.1103/PhysRevC.88.015802
- Miyatsu, T., Cheoun, M.-K., and Saito, K. (2015). Equation of State for Neutron Stars With Hyperons and Quarks in the Relativistic Hartree-fock Approximation. *Astrophys. J.* 813, 135. doi:10.1088/0004-637X/813/2/135
- Miyatsu, T., Cheoun, M.-K., and Saito, K. (2022b). Asymmetric Nuclear Matter in Relativistic Mean-field Models with Isoscalar- and Isovector-meson Mixing. *Astrophys. J.* 929, 82. doi:10.3847/1538-4357/1929/1/ac5f40

- Miyatsu, T., Katayama, T., and Saito, K. (2012). Effects of Fock term, tensor coupling and baryon structure variation on a neutron star. *Phys. Lett. B* 709, 242–246. doi:10.1016/j.physletb.2012.02.009
- Miyatsu, T., Yamamuro, S., and Nakazato, K. (2013b). A new equation of state for neutron star matter with nuclei in the crust and hyperons in the core. *Astrophys. J.* 777, 4. doi:10.1088/0004-637X/777/1/4
- Most, E. R., Weih, L. R., Rezzolla, L., and Schaffner-Bielich, J. (2018). New constraints on radii and tidal deformabilities of neutron stars from GW170817. *Phys. Rev. Lett.* 120, 261103. doi:10.1103/PhysRevLett.120.261103
- Moustakidis, C. C., Niksic, T., Lalazissis, G. A., Vretenar, D., and Ring, P. (2010). Constraints on the inner edge of neutron star crusts from relativistic nuclear energy density functionals. *Phys. Rev. C* 81, 065803. doi:10.1103/PhysRevC.81.065803
- Mueller, H. and Serot, B. D. (1996). Relativistic mean field theory and the high density nuclear equation of state. *Nucl. Phys. A* 606, 508–537. doi:10.1016/0375-9474(96)00187-X
- Nagai, S., Miyatsu, T., Saito, K., and Tsushima, K. (2008). Quark-meson coupling model with the cloudy bag. *Phys. Lett. B* 666, 239–244. doi:10.1016/j.physletb.2008.07.065
- Negele, J. W. and Vautherin, D. (1973). Neutron star matter at subnuclear densities. *Nucl. Phys. A* 207, 298–320. doi:10.1016/0375-9474(73)90349-7
- Niksic, T., Vretenar, D., Finelli, P., and Ring, P. (2002). Relativistic Hartree-Bogolyubov model with density dependent meson nucleon couplings. *Phys. Rev. C* 66, 024306. doi:10.1103/PhysRevC.66.024306
- Oertel, M., Hempel, M., Klähn, T., and Typel, S. (2017). Equations of state for supernovae and compact stars. *Rev. Mod. Phys.* 89, 015007. doi:10.1103/RevModPhys.89.015007
- Oliinychenko, D., Sorensen, A., Koch, V., and McLerran, L. (2023). Sensitivity of Au+Au collisions to the symmetric nuclear matter equation of state at 2–5 nuclear saturation densities. *Phys. Rev. C* 108, 034908. doi:10.1103/PhysRevC.108.034908
- Oppenheimer, J. R. and Volkoff, G. M. (1939). On massive neutron cores. *Phys. Rev.* 55, 374–381. doi:10.1103/PhysRev.55.374
- Page, D., Geppert, U., and Weber, F. (2006). The Cooling of compact stars. *Nucl. Phys. A* 777, 497–530. doi:10.1016/j.nuclphysa.2005.09.019
- Patra, N. K., Venneti, A., Imam, S. M. A., Mukherjee, A., and Agrawal, B. K. (2023). Systematic analysis of the impacts of symmetry energy parameters on neutron star properties. *Phys. Rev. C* 107, 055804. doi:10.1103/PhysRevC.107.055804
- Piekarewicz, J. (2014). Symmetry Energy Constraints from Giant Resonances: A Theoretical Overview. *Eur. Phys. J. A* 50, 25. doi:10.1140/epja/i2014-14025-x
- Pradhan, B. K., Chatterjee, D., Gandhi, R., and Schaffner-Bielich, J. (2023). Role of vector self-interaction in neutron star properties. *Nucl. Phys. A* 1030, 122578. doi:10.1016/j.nuclphysa.2022.122578
- Providência, C., Avancini, S. S., Cavagnoli, R., Chiacchiera, S., Ducoin, C., Grill, F., et al. (2014). Imprint of the symmetry energy on the inner crust and strangeness content of neutron stars. *Eur. Phys. J. A* 50, 44. doi:10.1140/epja/i2014-14044-7
- Psonis, V. P., Moustakidis, C. C., and Massen, S. E. (2007). Nuclear symmetry energy effects on neutron stars properties. *Mod. Phys. Lett. A* 22, 1233–1254. doi:10.1142/S0217732307023572
- Raithel, C., Özel, F., and Psaltis, D. (2018). Tidal deformability from GW170817 as a direct probe of the neutron star radius. *Astrophys. J. Lett.* 857, L23. doi:10.3847/2041-8213/aabcbf
- Reed, B. T., Fattoyev, F. J., Horowitz, C. J., and Piekarewicz, J. (2021). Implications of PREX-2 on the Equation of State of Neutron-Rich Matter. *Phys. Rev. Lett.* 126, 172503. doi:10.1103/PhysRevLett.126.172503

- Reed, B. T., Fattoyev, F. J., Horowitz, C. J., and Piekarewicz, J. (2024). Density dependence of the symmetry energy in the post-PREX-CREX era. *Phys. Rev. C* 109, 035803. doi:10.1103/PhysRevC.109.035803
- Reinhard, P.-G., Roca-Maza, X., and Nazarewicz, W. (2021). Information Content of the Parity-Violating Asymmetry in Pb208. *Phys. Rev. Lett.* 127, 232501. doi:10.1103/PhysRevLett.127.232501
- Reinhard, P. G., Rufa, M., Maruhn, J., Greiner, W., and Friedrich, J. (1986). Nuclear Ground State Properties in a Relativistic Meson Field Theory. *Z. Phys. A* 323, 13–25
- Richter, J. and Li, B.-A. (2023). Empirical radius formulas for canonical neutron stars from bidirectionally selecting features of equations of state in extended Bayesian analyses of observational data. *Phys. Rev. C* 108, 055803. doi:10.1103/PhysRevC.108.055803
- Riley, T. E. et al. (2019). A NICER View of PSR J0030+0451: Millisecond Pulsar Parameter Estimation. *Astrophys. J. Lett.* 887, L21. doi:10.3847/2041-8213/ab481c
- Riley, T. E. et al. (2021). A NICER View of the Massive Pulsar PSR J0740+6620 Informed by Radio Timing and XMM-Newton Spectroscopy. *Astrophys. J. Lett.* 918, L27. doi:10.3847/2041-8213/ac0a81
- Ring, P. (1996). Relativistic mean field in finite nuclei. *Prog. Part. Nucl. Phys.* 37, 193–263. doi:10.1016/0146-6410(96)00054-3
- Routray, T. R., Viñas, X., Basu, D. N., Pattnaik, S. P., Centelles, M., Robledo, L., et al. (2016). Exact versus Taylor-expanded energy density in the study of the neutron star crust–core transition. *J. Phys. G* 43, 105101. doi:10.1088/0954-3899/43/10/105101
- Rutherford, N. et al. (2024). Constraining the Dense Matter Equation of State with New NICER Mass–Radius Measurements and New Chiral Effective Field Theory Inputs. *Astrophys. J. Lett.* 971, L19. doi:10.3847/2041-8213/ad5f02
- Saito, K., Miyatsu, T., and Cheoun, M.-K. (2024). Effect of isoscalar and isovector scalar fields on baryon semileptonic decays in nuclear matter. arXiv:2409.14764. doi:10.48550/arXiv.2409.14764
- Saito, K. and Thomas, A. W. (1994a). A Quark - meson coupling model for nuclear and neutron matter. *Phys. Lett. B* 327, 9–16. doi:10.1016/0370-2693(94)91520-2
- Saito, K. and Thomas, A. W. (1994b). The Nolen-Schiffer anomaly and isospin symmetry breaking in nuclear matter. *Phys. Lett. B* 335, 17–23. doi:10.1016/0370-2693(94)91551-2
- Saito, K., Tsushima, K., and Thomas, A. W. (2007). Nucleon and hadron structure changes in the nuclear medium and impact on observables. *Prog. Part. Nucl. Phys.* 58, 1–167. doi:10.1016/j.pnpnp.2005.07.003
- Salinas, M. and Piekarewicz, J. (2023a). Bayesian refinement of covariant energy density functionals. *Phys. Rev. C* 107, 045802. doi:10.1103/PhysRevC.107.045802
- Salinas, M. and Piekarewicz, J. (2023b). Building an Equation of State Density Ladder. *Symmetry* 15, 994. doi:10.3390/sym15050994
- Serot, B. D. and Walecka, J. D. (1986). The Relativistic Nuclear Many Body Problem. *Adv. Nucl. Phys.* 16, 1–327
- Sharma, M. M. (2008). Scalar-vector Lagrangian without nonlinear self-interactions of bosonic fields in the relativistic mean-field theory. *Phys. Lett. B* 666, 140–144. doi:10.1016/j.physletb.2008.07.005
- Sotani, H. and Ota, S. (2022). Neutron star mass formula with nuclear saturation parameters for asymmetric nuclear matter. *Phys. Rev. D* 106, 103005. doi:10.1103/PhysRevD.106.103005
- Stone, J. R. (2021). Nuclear Physics and Astrophysics Constraints on the High Density Matter Equation of State. *Universe* 7, 257. doi:10.3390/universe7080257
- Stone, J. R. (2024). Nuclear Symmetry Energy in Strongly Interacting Matter: Past, Present and Future. *Symmetry* 16, 1038. doi:10.3390/sym16081038
- Sugahara, Y. and Toki, H. (1994). Relativistic mean field theory for unstable nuclei with nonlinear sigma and omega terms. *Nucl. Phys. A* 579, 557–572. doi:10.1016/0375-9474(94)90923-7

- Sulaksono, A., Alam, N., and Agrawal, B. K. (2014). Core–crust transition properties of neutron stars within systematically varied extended relativistic mean-field model. *Int. J. Mod. Phys. E* 23, 1450072. doi:10.1142/S0218301314500724
- Sun, B., Bhattiprolu, S., and Lattimer, J. M. (2024). Compiled properties of nucleonic matter and nuclear and neutron star models from nonrelativistic and relativistic interactions. *Phys. Rev. C* 109, 055801. doi:10.1103/PhysRevC.109.055801
- Tamii, A. et al. (2011). Complete electric dipole response and the neutron skin in ^{208}Pb . *Phys. Rev. Lett.* 107, 062502. doi:10.1103/PhysRevLett.107.062502
- Tarbert, C. M. et al. (2014). Neutron skin of ^{208}Pb from Coherent Pion Photoproduction. *Phys. Rev. Lett.* 112, 242502. doi:10.1103/PhysRevLett.112.242502
- Todd-Rutel, B. G. and Piekarewicz, J. (2005). Neutron-Rich Nuclei and Neutron Stars: A New Accurately Calibrated Interaction for the Study of Neutron-Rich Matter. *Phys. Rev. Lett.* 95, 122501. doi:10.1103/PhysRevLett.95.122501
- Tolman, R. C. (1939). Static solutions of Einstein's field equations for spheres of fluid. *Phys. Rev.* 55, 364–373. doi:10.1103/PhysRev.55.364
- Tsang, C. Y., Tsang, M. B., Lynch, W. G., Kumar, R., and Horowitz, C. J. (2024). Determination of the equation of state from nuclear experiments and neutron star observations. *Nature Astron.* 8, 328–336. doi:10.1038/s41550-023-02161-z
- Tsang, M. B., Zhang, Y., Danielewicz, P., Famiano, M., Li, Z., Lynch, W. G., et al. (2009). Constraints on the density dependence of the symmetry energy. *Phys. Rev. Lett.* 102, 122701. doi:10.1103/PhysRevLett.102.122701
- Tsang, M. B. et al. (2012). Constraints on the symmetry energy and neutron skins from experiments and theory. *Phys. Rev. C* 86, 015803. doi:10.1103/PhysRevC.86.015803
- Typel, S. and Brown, B. A. (2001). Neutron radii and the neutron equation of state in relativistic models. *Phys. Rev. C* 64, 027302. doi:10.1103/PhysRevC.64.027302
- Xie, W.-J. and Li, B.-A. (2019). Bayesian Inference of High-density Nuclear Symmetry Energy from Radii of Canonical Neutron Stars. *Astrophys. J.* 883, 174. doi:10.3847/1538-4357/ab3f37
- Xie, W.-J., Li, B.-A., and Zhang, N.-B. (2024). Impact of the newly revised gravitational redshift of x-ray burster GS 1826-24 on the equation of state of supradense neutron-rich matter. *Phys. Rev. D* 110, 043025. doi:10.1103/PhysRevD.110.043025
- Xu, J., Chen, L.-W., Li, B.-A., and Ma, H.-R. (2009). Nuclear constraints on properties of neutron star crusts. *Astrophys. J.* 697, 1549–1568. doi:10.1088/0004-637X/697/2/1549
- Zabari, N., Kubis, S., and Wójcik, W. (2019). Influence of the interactions of scalar mesons on the behavior of the symmetry energy. *Phys. Rev. C* 99, 035209. doi:10.1103/PhysRevC.99.035209
- Zenihiro, J. et al. (2010). Neutron density distributions of Pb-204, Pb-206, Pb-208 deduced via proton elastic scattering at $E_p=295$ MeV. *Phys. Rev. C* 82, 044611. doi:10.1103/PhysRevC.82.044611
- Zhang, N.-B. and Li, B.-A. (2021). Impact of NICER's Radius Measurement of PSR J0740+6620 on Nuclear Symmetry Energy at Suprasaturation Densities. *Astrophys. J.* 921, 111. doi:10.3847/1538-4357/ac1e8c
- Zhang, N.-B., Li, B.-A., and Xu, J. (2018). Combined Constraints on the Equation of State of Dense Neutron-rich Matter from Terrestrial Nuclear Experiments and Observations of Neutron Stars. *Astrophys. J.* 859, 90. doi:10.3847/1538-4357/aac027
- Zhou, J., Xu, J., and Papakonstantinou, P. (2023). Bayesian inference of neutron-star observables based on effective nuclear interactions. *Phys. Rev. C* 107, 055803. doi:10.1103/PhysRevC.107.055803